Supplementary Materials

High-performance, noninvasive flexible sensing array for gesture and handwriting recognition assisted by machine learning

Lu Liu[1,2,3,*], Hengxiang Liu[2], Shudan Li[1,3], Xinlu Wei[1,3], Jiantao Yao[1,3], Bo Han[1,3], Hao Zhou[1,3], Dianyu Wang[4], Yundou Xu[1,3,*], Xiaoli Jia[2,*]

[1]Parallel Robot and Mechatronic System Laboratory of Hebei Province, Yanshan University, Qinhuangdao 066004, Hebei, China.
[2]College of Mechanical and Transportation Engineering, China University of Petroleum-Beijing, Beijing 102249, China.
[3]Hebei Provincial National Defense Key Discipline Laboratory of General Technology on Military Basic Electromechanical Products, Yanshan University, Qinhuangdao 066004, Hebei, China.
[4]School of Chemical Engineering, Zhengzhou University, Zhengzhou 450001, Henan, China.

[*]**Correspondence to:** Dr. Lu Liu, Prof. Yundou Xu, Parallel Robot and Mechatronic System Laboratory of Hebei Province, Yanshan University, Qinhuangdao 066004, Hebei, China. E-mail: luliu@ysu.edu.cn; ydxu@ysu.edu.cn; Prof. Xiaoli Jia, College of Mechanical and Transportation Engineering, China University of Petroleum-Beijing, Beijing 102249, China. E-mail: xljia@cup.edu.cn

This supporting file includes:

- Supplementary Note 1-6
- Supplementary Figures 1-54
- Supplementary Tables 1-6.
- Supplementary Equations 1-8

The sequence is the same as they are mentioned in the main text.

Supplementary Note 1. Tendon coordination during handwriting

To provide anatomical context for the pressure variations measured during handwriting, the forearm flexor region was examined with reference to several representative muscles, including the flexor carpi radialis (FCR), palmaris longus (PL), flexor carpi ulnaris (FCU), flexor digitorum superficialis (FDS), flexor digitorum profundus (FDP), and flexor pollicis longus (FPL). These muscles participate in wrist flexion and finger motion during writing and collectively influence the mechanical state of the forearm tissues.

Different handwriting strokes may generate distinct patterns of forearm motion and tissue deformation. For example, rounded strokes such as the character “c” generally involve relatively smooth and continuous wrist and finger motion, which can produce a more symmetric deformation pattern in the surrounding soft tissues. In contrast, strokes containing vertical or downward segments such as “P” may involve different wrist postures and tendon movements, leading to a slightly asymmetric deformation pattern across the forearm tissues.

Although the flexible sensing array only contacts the skin surface, the underlying motion of muscles, tendons, and surrounding tissues can induce subtle pressure variations that propagate through the soft tissue layers and become detectable by the FMG sensors. These pressure patterns are closely related to the overall handwriting motion and stroke trajectory.

The schematic shown in Figure 1a illustrates possible forearm anatomical structures and representative deformation patterns associated with the writing of “c” and “P”. It should be noted that this illustration serves as an anatomical and conceptual reference for understanding the observed pressure patterns rather than a direct measurement of specific muscle activation.

Supplementary Note 2. Crosstalk origin and mitigation strategies

Crosstalk in the sensor array may arise from two primary sources: mechanical coupling, where deformation propagates through the compliant polydimethylsiloxane (PDMS) substrate, and electrical coupling, caused by lateral conductive pathways or shared readout interference.

To suppress these effects, multi-level design strategies are implemented. Structurally, each sensing unit is defined by a localized microstructured region to confine deformation and reduce stress transfer. At the material level, the multi-walled carbon nanotube (MWCNT) conductive layer is spatially restricted to individual units, preventing lateral conduction. At the circuit level, each channel is independently connected through separate readout pathways with series resistors to ensure electrical isolation. In addition, multi-channel spatiotemporal feature extraction further mitigates the influence of residual coupling.

These combined strategies effectively minimize crosstalk and enable reliable multi-channel signal acquisition.

Supplementary Note 3. Human trial protocol and ethical considerations

Human experiments were conducted to evaluate the performance of the wearable flexible sensor array in gesture and handwriting recognition. All participants were recruited on a voluntary basis from within the research group, and informed consent was obtained from all participants prior to the experiments. The study involved non-invasive, minimal-risk measurements, and no biological samples, medical interventions, or personal sensitive information were collected. The device was fabricated from biocompatible materials (e.g., PDMS and polyurethane film) and operated under safe electrical conditions. The sensor was attached to the inner forearm using medical-grade polyurethane film, which is widely used for skin-contact applications. No discomfort, skin irritation, or adverse effects were reported during the experiments. Participants were asked to perform predefined gesture and handwriting tasks under normal conditions. Each session lasted approximately 20 minutes, including rest periods to avoid fatigue. Given that the study involved minimal-risk, non-invasive procedures with voluntary participation and informed consent, and did not involve vulnerable populations or sensitive data, formal institutional ethical approval was not required according to local regulations.

Supplementary Note 4. Network training details and validation

The dataset was randomly partitioned into a training set (80%) and a test set (20%) to ensure an unbiased evaluation of model performance. Within each training split, 10% of the samples were further separated as a validation set for hyperparameter tuning and training monitoring.

The deep neural network (DNN) consisted of three fully connected hidden layers with 50, 30, and 20 neurons, respectively. Batch normalization and dropout (dropout rate = 0.2) were applied after the first two layers to enhance training stability and mitigate overfitting. The model was trained using the Adam optimizer with an initial learning rate of 1×10^{-3}, a mini-batch size of 32, and a maximum of 150 epochs. A piecewise learning-rate decay schedule was adopted with a drop factor of 0.5 every 10 epochs. All input features were normalized based on training-set statistics to avoid information leakage. The network weights were initialized using the default MATLAB settings, and no explicit L2 regularization term was introduced. Training was conducted on a workstation equipped with an Intel i9-13900K CPU and an NVIDIA RTX 4090 GPU. The model typically converged within approximately 95 s, achieving stable accuracy and recall without observable overfitting, as evidenced by the training curves (Figures 6(b–g)). The relatively short training time highlights the computational efficiency of the proposed framework, enabling rapid retraining for subject-specific calibration or adaptation to extended motion classes in practical applications.

Supplementary Note 5. Interdisciplinary consistency and recalibration

To evaluate the robustness between individuals, cross subject validation was conducted using the Leave One Subject (LOSO) protocol. When the model trained on data from 9 participants was tested on the remaining participant, the average recognition accuracy decreased from 99.5% (within the subjects) to 97.8% (across subjects), indicating a high degree of generalization ability between individuals (Figures S44a and b). The decrease in small precision is mainly due to changes in muscle morphology and forearm circumference, which slightly alter the pressure distribution on the sensing array. Due to the minimal baseline drift (<2%) and stable sensitivity exhibited by the array under repeated attachment, there is no need for complete retraining of the neural network; Only use lightweight device calibration routines to update normalization parameters.

These results confirm that the proposed system maintains reliable classification performance across different users and repeated wearing cycles, highlighting its robustness to everyday wearable applications.

Supplementary Note 6. Robustness to handwriting continuity, style, and scale

To further evaluate the temporal and morphological adaptability of the system, we examined the recognition performance under three writing conditions: discrete handwriting, continuous cursive writing, and rapid stylized writing. The trained model maintained a high classification accuracy of 98.7 % for cursive scripts and 97.9 % for high-speed writing, with only a minor decrease (< 1.5 %) compared with discrete characters. This indicates that the force–temporal signatures captured by the nine-channel array remain distinguishable even when stroke boundaries overlap in time.

The model does not require the user to pause between characters; instead, it performs continuous dynamic segmentation through short-time Fourier and statistical feature extraction, allowing real-time decoding of fluent handwriting without perceptible delay. Variations in handwriting size and personal style were further analyzed by scaling experiments, where the same subjects wrote with character sizes ranging from 5 mm to 25 mm. The recognition accuracy remained above 97 %, owing to the relative invariance of muscle deformation patterns with respect to geometric scaling. These results suggest that the proposed FMG-based approach generalizes across different handwriting speeds, scales, and stylistic variations, effectively bridging discrete and cursive writing modes and enabling fluid interaction in practical applications.

Sensitivity calculation formula of flexible pressure sensing unit[16-18]

$$S = \frac{\Delta I / I_0}{\Delta P} \tag{S2}$$

$$\Delta I = I - I_0 \tag{S3}$$

$$\Delta P = P - P_0 \tag{S4}$$

$$R^2 = 1 - \frac{\sum_{i=1}^{n} \left(y_{\mathrm{i}} - \widehat{y_{\mathrm{i}}} \right)^2}{\sum_{i=1}^{n} \left(y_{\mathrm{i}} - \bar{y} \right)^2} \tag{S5}$$

where I is the real-time current, I_0 is the initial current, P is the real-time stress acting on the sensor, P_0 is the initial stress acting on the sensor, y_{i} is the actual measured value, $\widehat{y_{\mathrm{i}}}$ is the model fitting value, and $\bar{y}$ is the mean of the actual measured values.

Sensitivity error of sensors from different batches[16-18]

$$S_{\mathrm{r}} = \frac{S_{\mathrm{i}} - \bar{S}}{\bar{S}} \times 100\% \tag{S6}$$

where S_{i} is the sensitivity of sensors from different batches, and $\bar{S}$ is the mean sensitivity of sensors from different batches.

Linearity error [16-18]

$$\delta_L = \frac{\max \left| y_{\mathrm{i}} - y_{\mathrm{ni}} \right|}{y_{\max}} \times 100\% \tag{S7}$$

where y_{i} is the actual output at a certain input value, y_{ni} is the ideal output of the sensor at the same input value (based on a calibrated or fitted linear model), and $y_{\max}$ is the full-scale output value of the sensor.

Repeatability error[16-18]

$$\delta_{\mathrm{R}} = \frac{\max \left| y_{\mathrm{i}} - \bar{y} \right|}{y_{\max}} \times 100\% \tag{S8}$$

where $\bar{y}$ is the output mean of a certain input value in multiple measurements.

Hysteresis Error[16-18]

$$\delta_{\mathrm{H}}=\frac{\max\left|y_{\mathrm{s}}-y_{x}\right|}{y_{\max}}\times 100\% \tag{S8}$$

where y_{s} is the output for a certain input value during loading, and y_{x} is the output for the same input value during unloading.

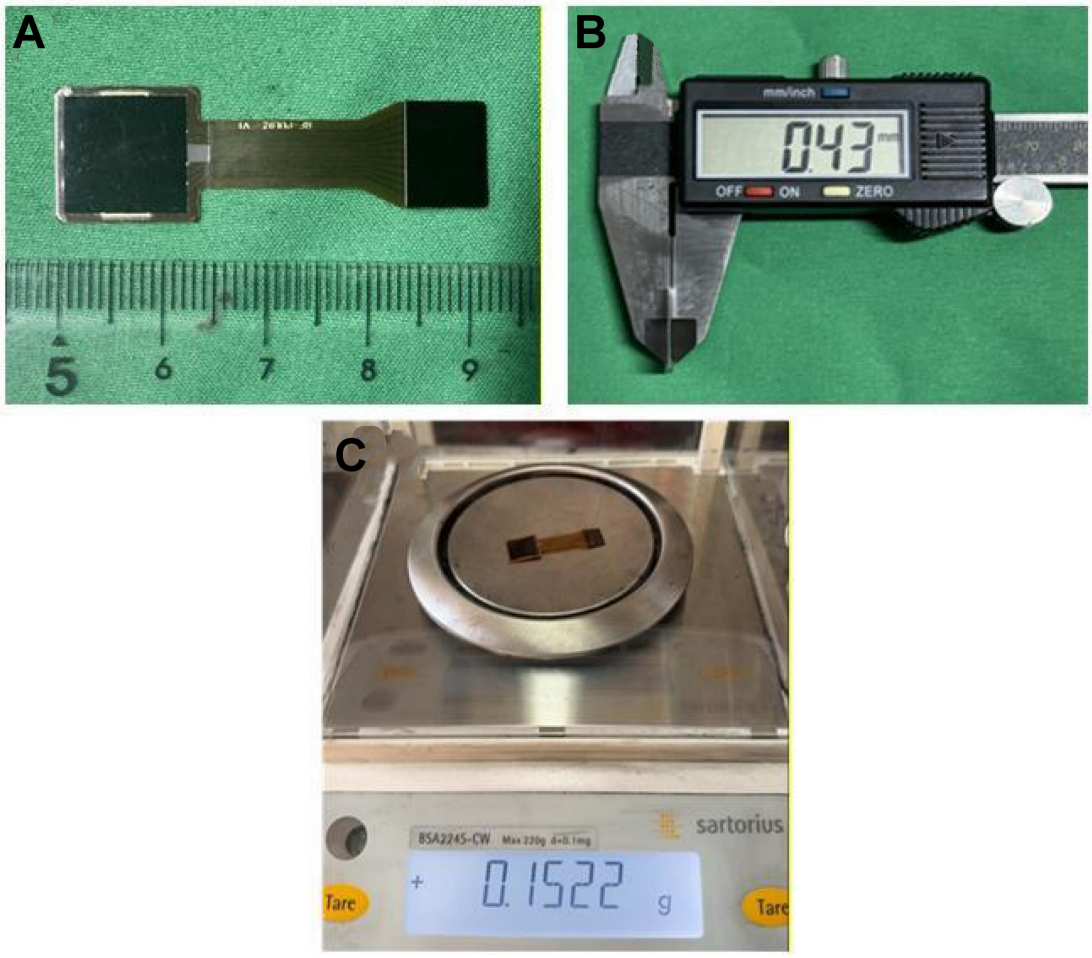

Supplementary Figure 1. (A) Physical image, (B) thickness and (C) mass of the flexible sensor array.

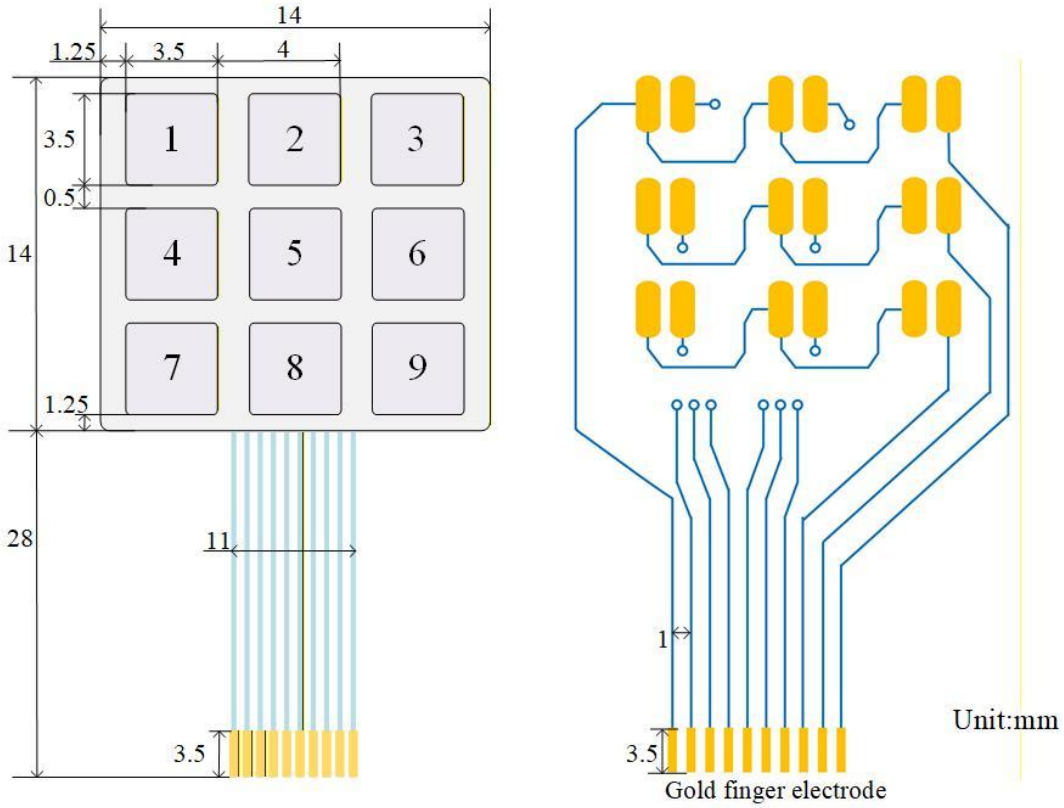

Supplementary Figure 2. Dimensions of flexible sensor array and design of flexible electrodes.

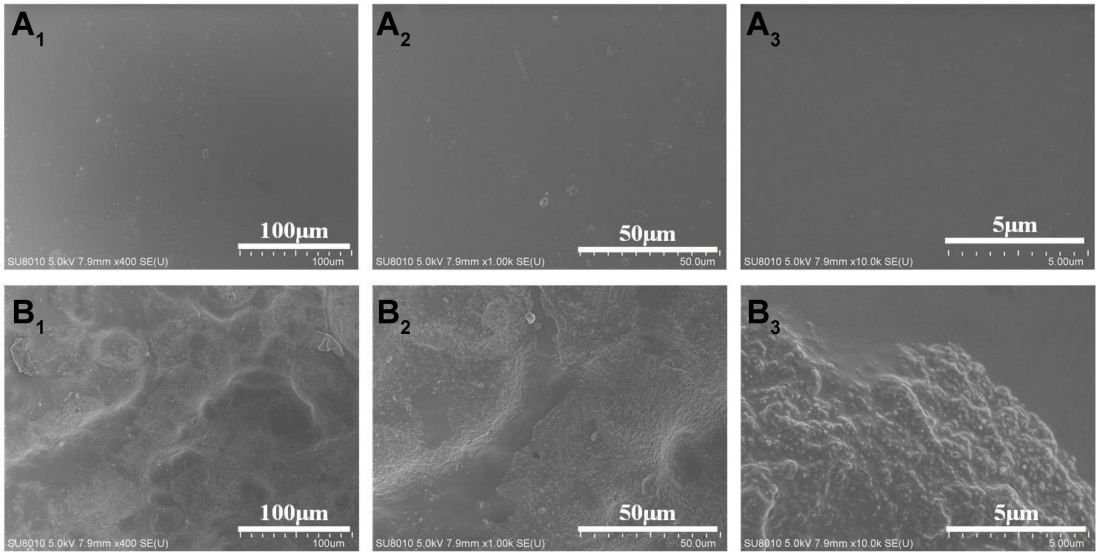

Supplementary Figure 3. SEM images at different magnifications (A) PDMS and (B) MWCNTs/PDMS.

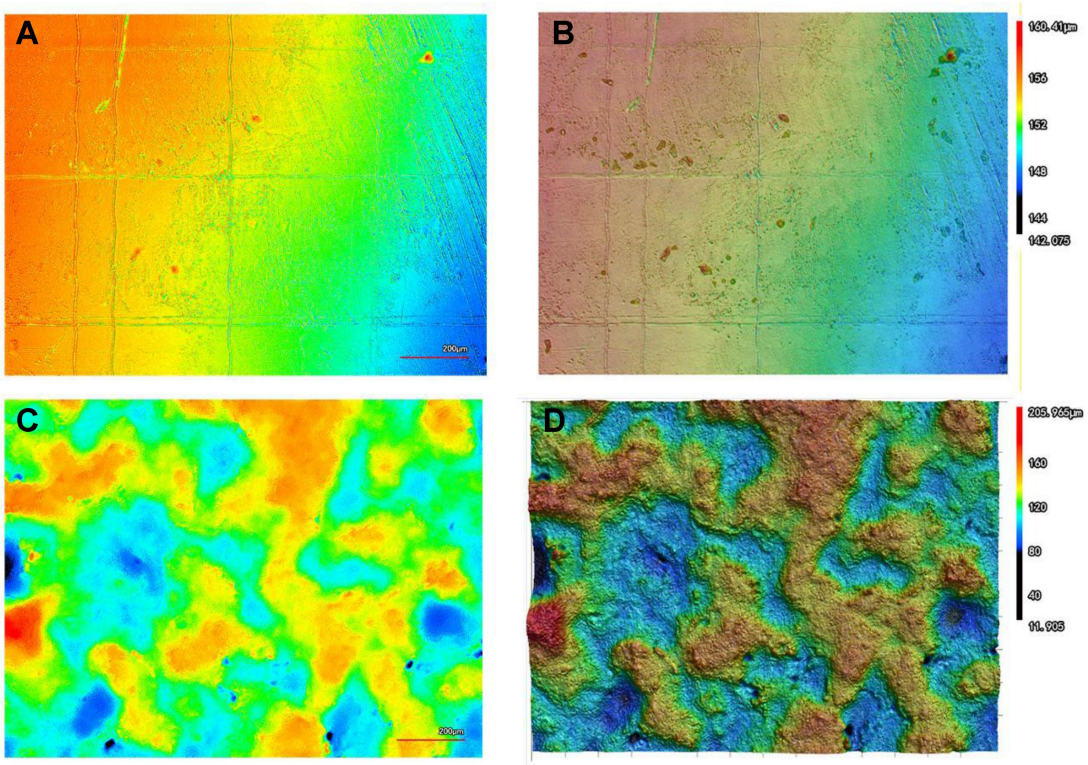

Supplementary Figure 4. 3D topography scanning photos (A), (B) PDMS and (C), (D) MWCNTs/PDMS.

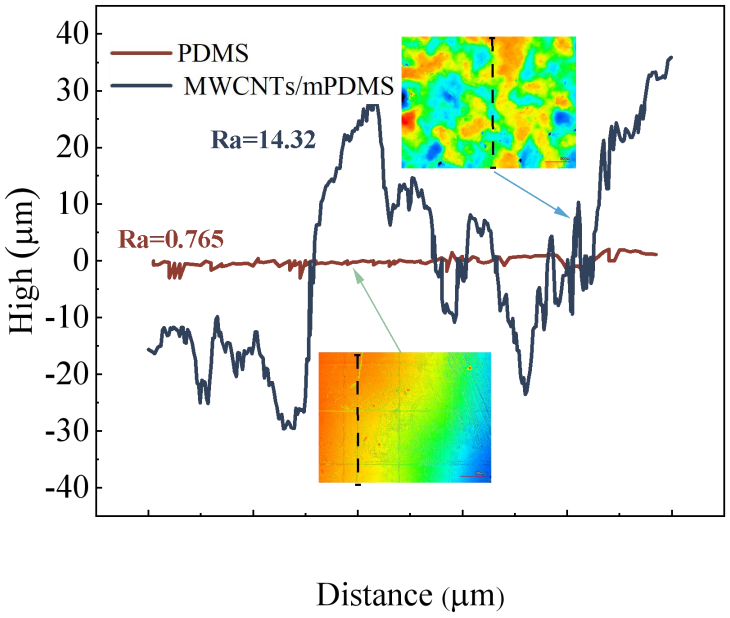

Supplementary Figure 5. Surface roughness of PDMS and MWCNTs/PDMS.

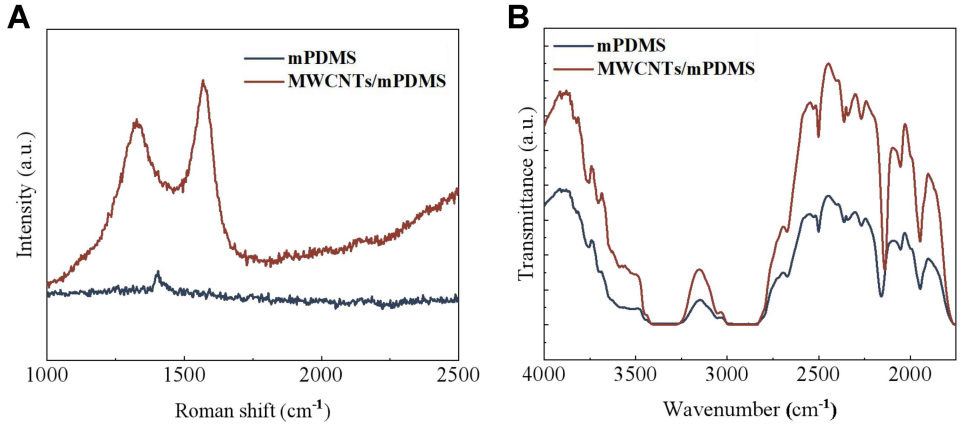

Supplementary Figure 6. (A) Raman spectrum and (B) Fourier transform infrared spectrum of MWCNTs/PDMS.

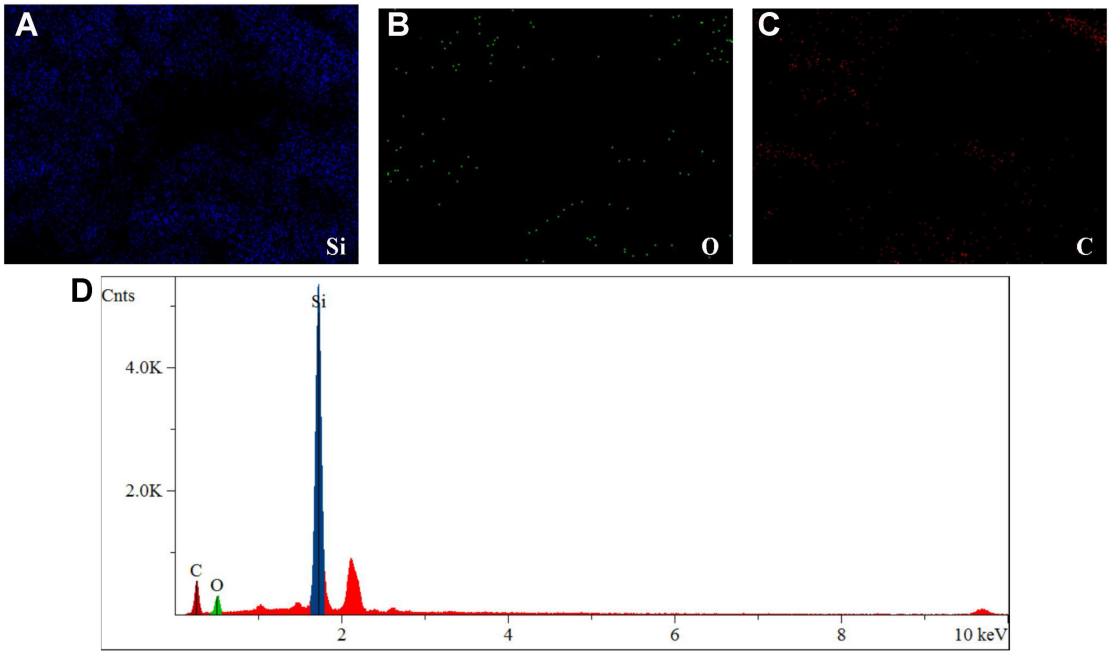

Supplementary Figure 7. Element distribution and energy spectrum of MWCNTs.

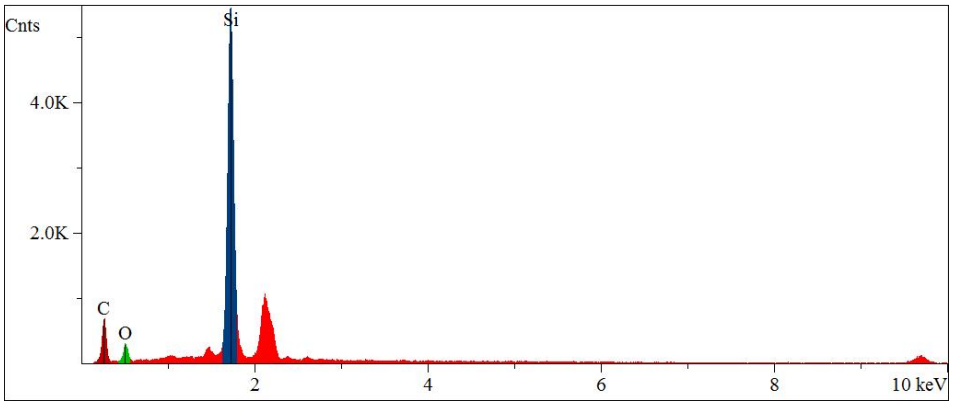

Supplementary Figure 8. MWCMTs/mPDMS energy spectrum.

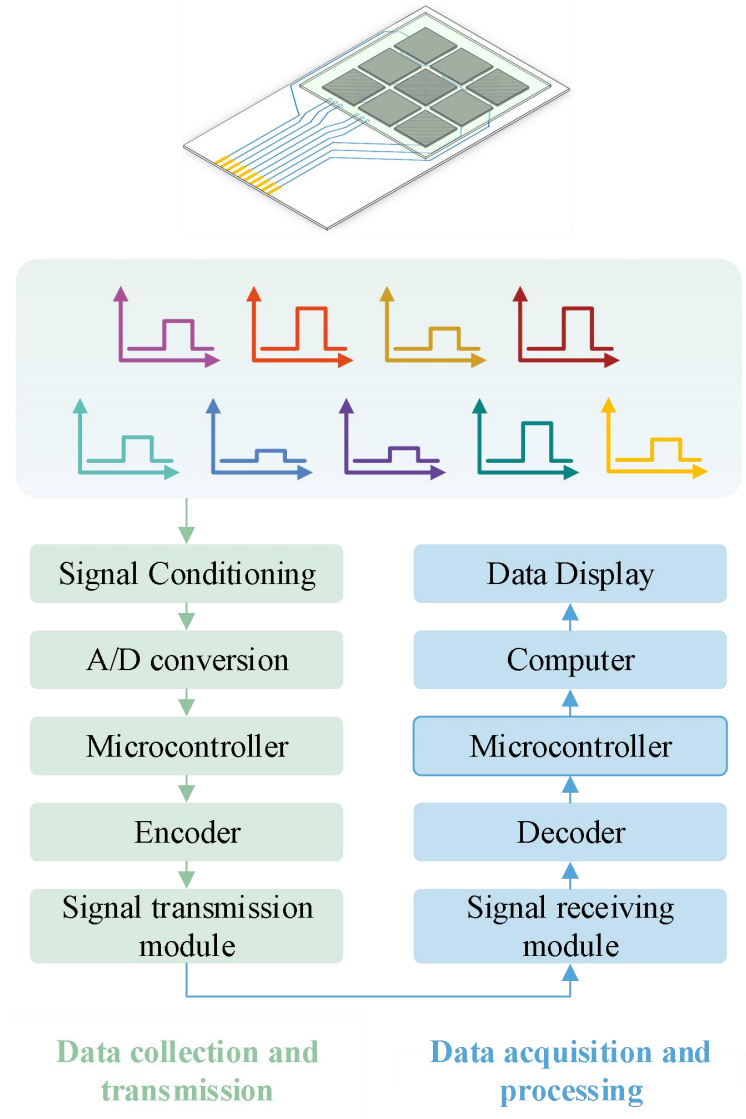

Supplementary Figure 9. Block diagram of wireless sensor data collection and transmission.

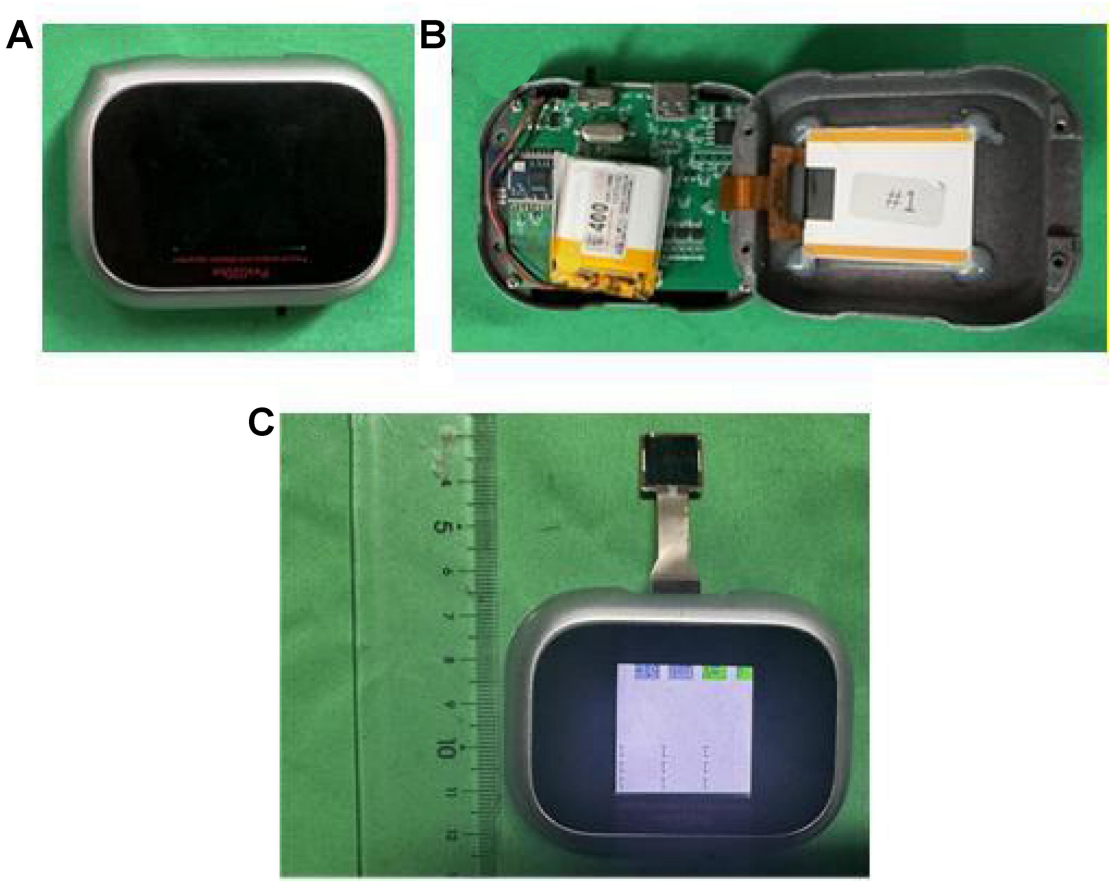

Supplementary Figure 10. Actual picture of wireless transmission module.

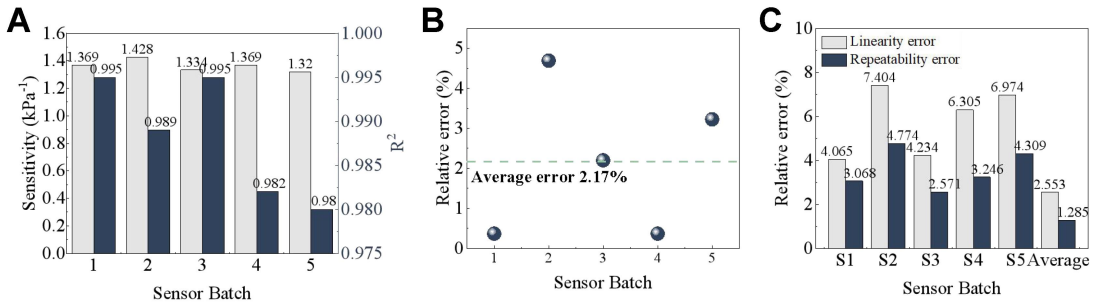

Supplementary Figure 11. Performance characterization of sensors from different batches. (A) Sensitivity, (B) sensitivity relative error, (C) linearity error and repeatability error.

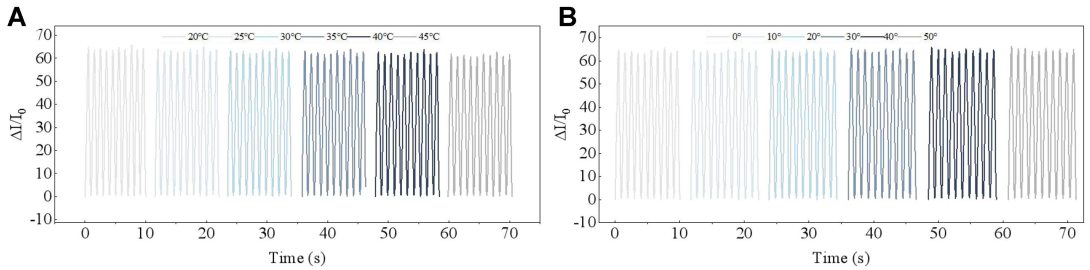

Supplementary Figure 12. Environmental and mechanical stability of the sensor. (A) Temperature dependence; (B) Bending dependence. To evaluate the stability of the sensor in real-world usage environments, tests were conducted on its electrical response under different temperature and bending conditions. In the temperature test, the sensor was placed in a controlled temperature environment (20-45°C), and its current change signal ($\Delta I/I_0$) was recorded under constant pressure loading conditions. After stabilizing at each temperature point (approximately 2–3 minutes), multiple sets of data were collected and averaged, while the standard deviation was calculated as the error bar. In the bending test, different bending angles were applied through a controllable bending device to simulate structural deformation caused by limb movement during actual wear. The electrical response of the sensor was collected in real-time under dynamic bending conditions to evaluate its stability and structural adaptability during deformation. Measurements were repeated multiple times at each bending radius, and the average value and standard deviation were calculated. All electrical signals were recorded in real-time using a digital multimeter to ensure the acquisition of the sensor's immediate response during environmental changes and mechanical deformation (rather than the recovery signal after deformation).

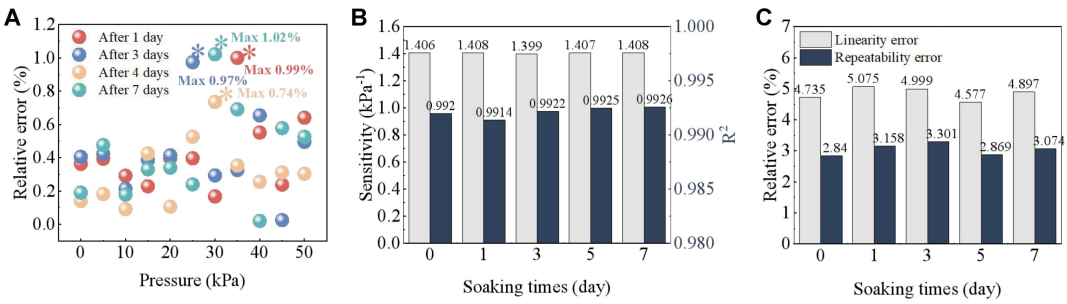

Supplementary Figure 13. (A) Relative error of response under different pressures, (B) sensitivity, (C) linearity error and repeatability error of the flexible sensor unit after immersion for different times.

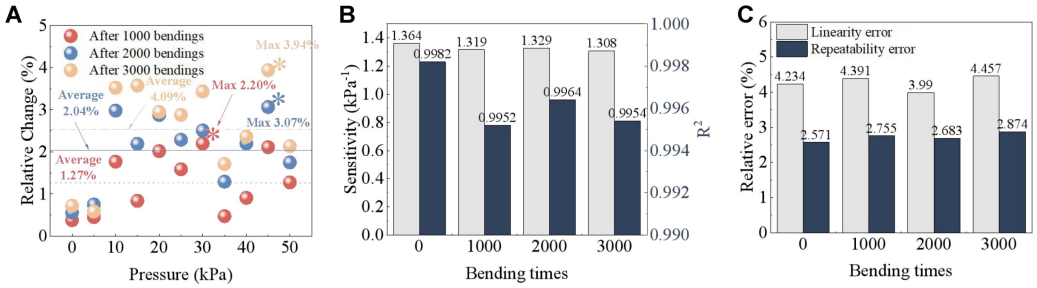

Supplementary Figure 14. (A) Relative error of response under different pressures, (B) sensitivity, (C) linearity error and repeatability error of the flexible sensor unit after bending for different times.

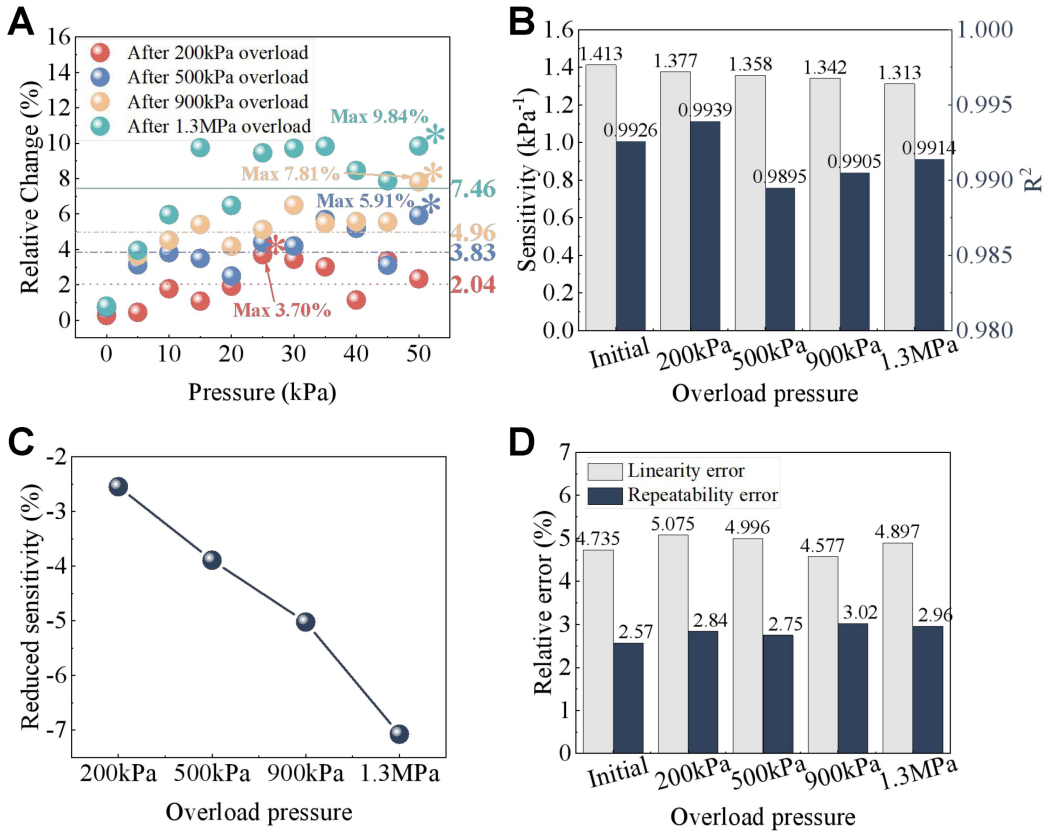

Supplementary Figure 15. (A) Relative error of response under different pressures, (B) sensitivity, (C) relative change of sensitivity, (D) linearity error and repeatability error of the flexible sensor unit after different pressure overloads.

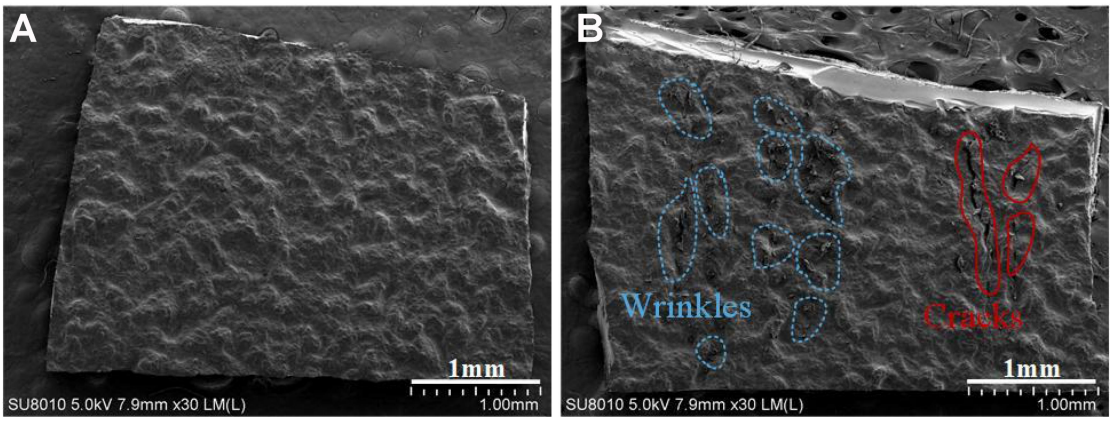

Supplementary Figure 16. (A) SEM image of MWCNTs/mPDMS without overload, (B) SEM image after 1.3 MPa overload.

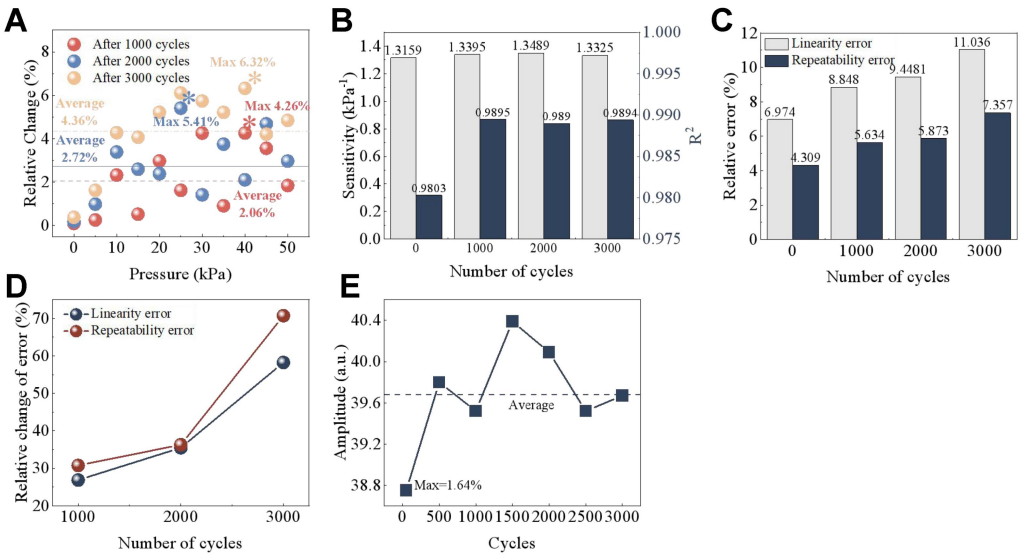

Supplementary Figure 17. Flexible sensing unit after cyclic loading for different number of times at 30 kPa pressure (A) relative error of response at different pressures, (B) sensitivity, (C) relative change of sensitivity, (D) linearity error and repeatability error, (E) Cyclic stability of signal amplitude under repeated loading.

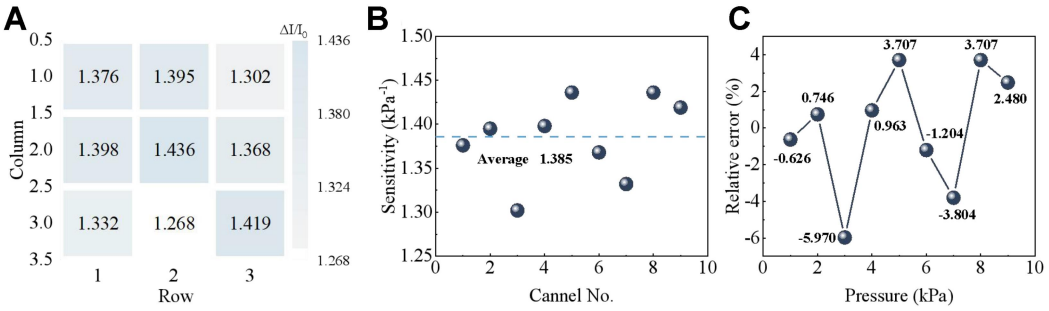

Supplementary Figure 18. Characterization of the sensitivity of the flexible sensing array. (A), (B) different channel sensitivities and their mean values, (C) error of different channel sensitivities relative to the mean value.

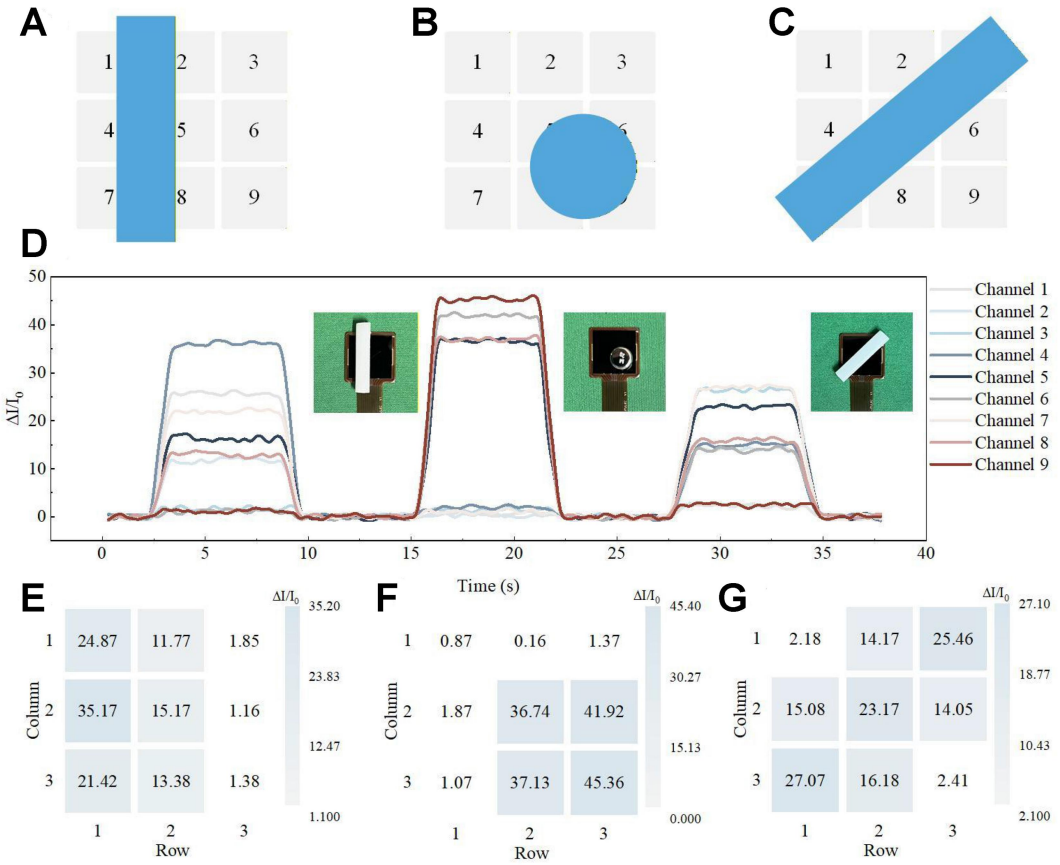

Supplementary Figure 19. Multi-point response characterization of the flexible sensing array. (A)~(C) Schematic of different external force loading, (D) Response curves of each channel, (E)~(F) Response thermograms of each channel.

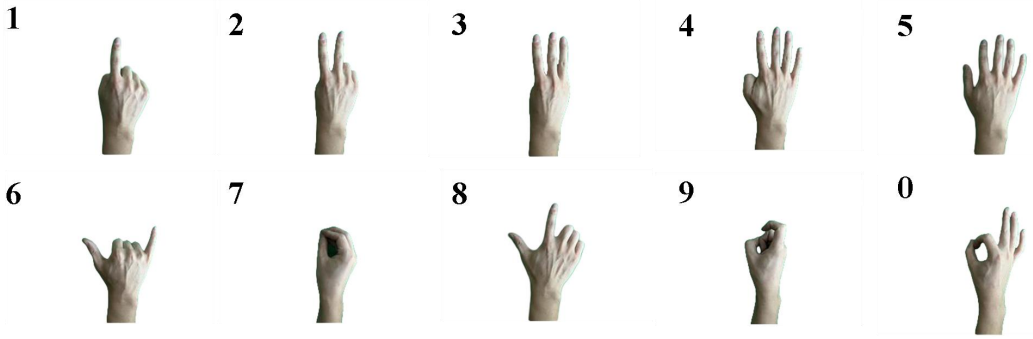

Supplementary Figure 20. Schematic diagram of different gesture movements.

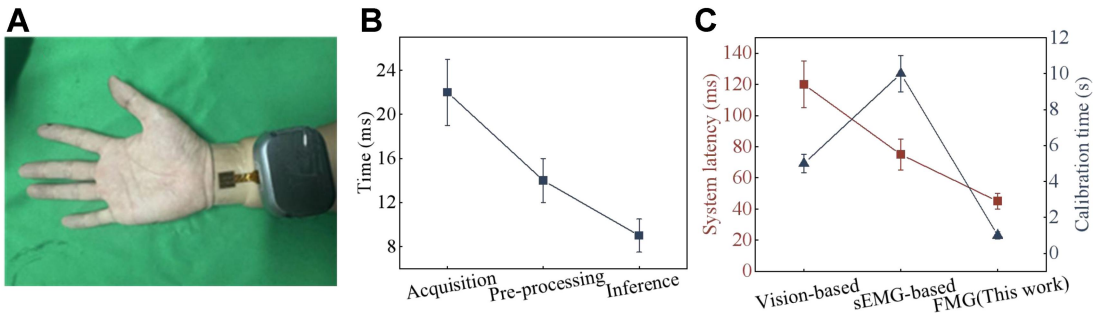

Supplementary Figure 21. (A) Location of the sensing array arrangement, (B) System latency breakdown of the proposed FMG-based handwriting recognition system, (C) Comparison of system latency and calibration time for different wearable handwriting interfaces. Error bars represent the standard deviation (SD) calculated from repeated measurements (n=5). Although the primary flexor muscles are located on the ventral side of the forearm, their contraction produces volumetric tissue deformation that propagates through the forearm tissues and can be detected by surface pressure sensors placed on the dorsal side. To evaluate the real-time performance of the system, a decomposition analysis was conducted on the overall delay, encompassing three stages: signal acquisition, preprocessing, and model inference (Figure S21b). The signal acquisition stage is primarily determined by the sampling window, while the preprocessing stage involves signal normalization and feature extraction. The model inference stage corresponds to the forward propagation process of the trained model. The results indicate that the total system delay is approximately 45 ms, satisfying the requirements for real-time human-computer interaction.The delay data for visual methods and sEMG methods are estimated based on existing literature reports and typical system processing workflows, including signal acquisition, preprocessing, and model inference [23,30,42]. Among them, due to the involvement of image acquisition and complex calculations, the delay of visual methods is usually greater than 100 ms; while the delay of sEMG methods ranges from tens to hundreds of milliseconds depending on the complexity of processing.The delay of the FMG system in this paper (approximately 45 ms) is derived from experimental analysis results, including signal acquisition, preprocessing, and model inference (see Figure S21c). Calibration time is defined as the total preparation time required by the system before effective data collection, including sensor/device installation, system initialization, and signal stabilization process. For visual methods, calibration mainly involves camera position adjustment and environmental setup,

typically taking about 5 minutes [23,42]; for sEMG methods, the calibration process includes electrode attachment, skin preparation, and signal conditioning, typically taking about 10 minutes [30]. The calibration time of the FMG system in this paper (about 1 minute) is derived from the experimental process, requiring only simple wearing and no conductive interface or repeated debugging.

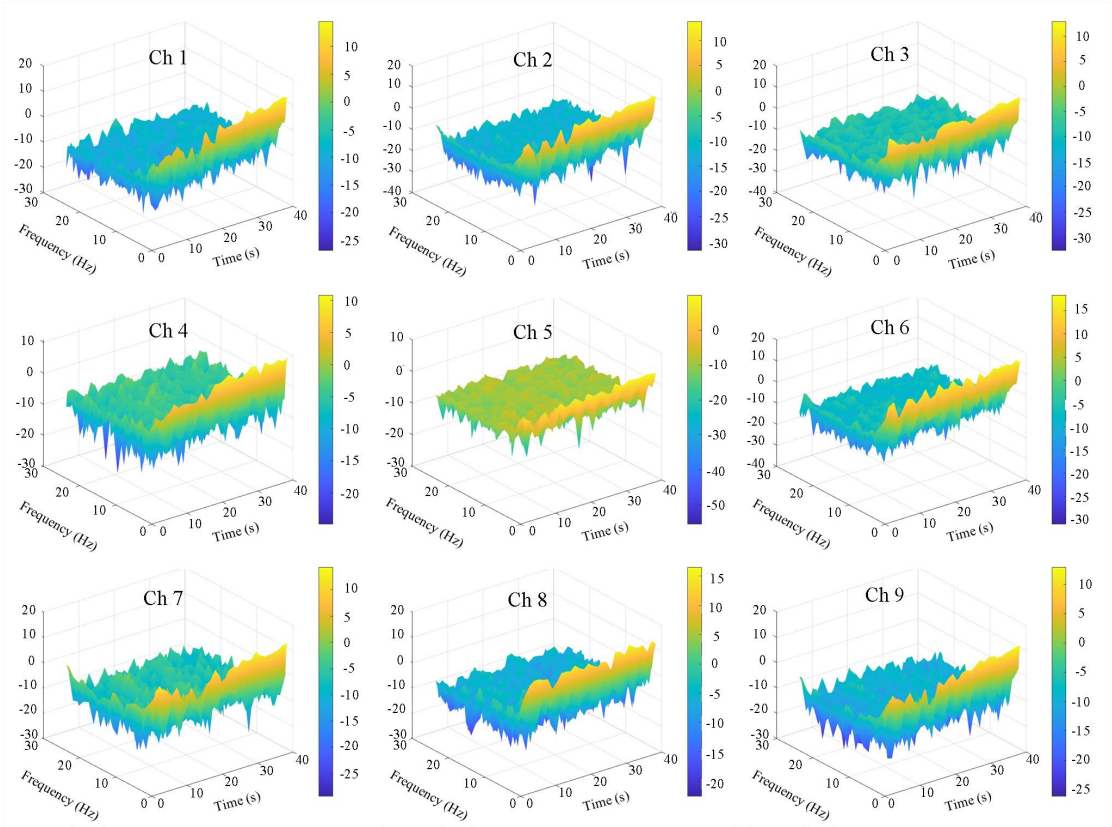

Supplementary Figure 22. Short-Time Fourier Transform (STFT) spectra of each channel's response to the digital 0 gesture.

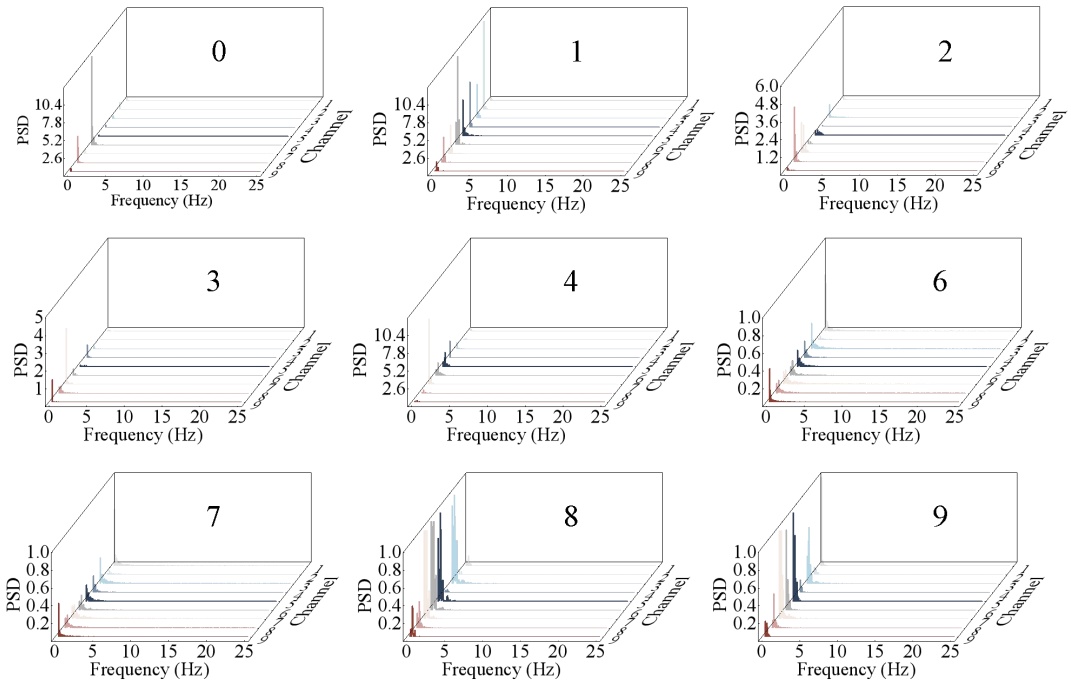

Supplementary Figure 23. Power spectral density (PSD) of each channel for different hand movements.

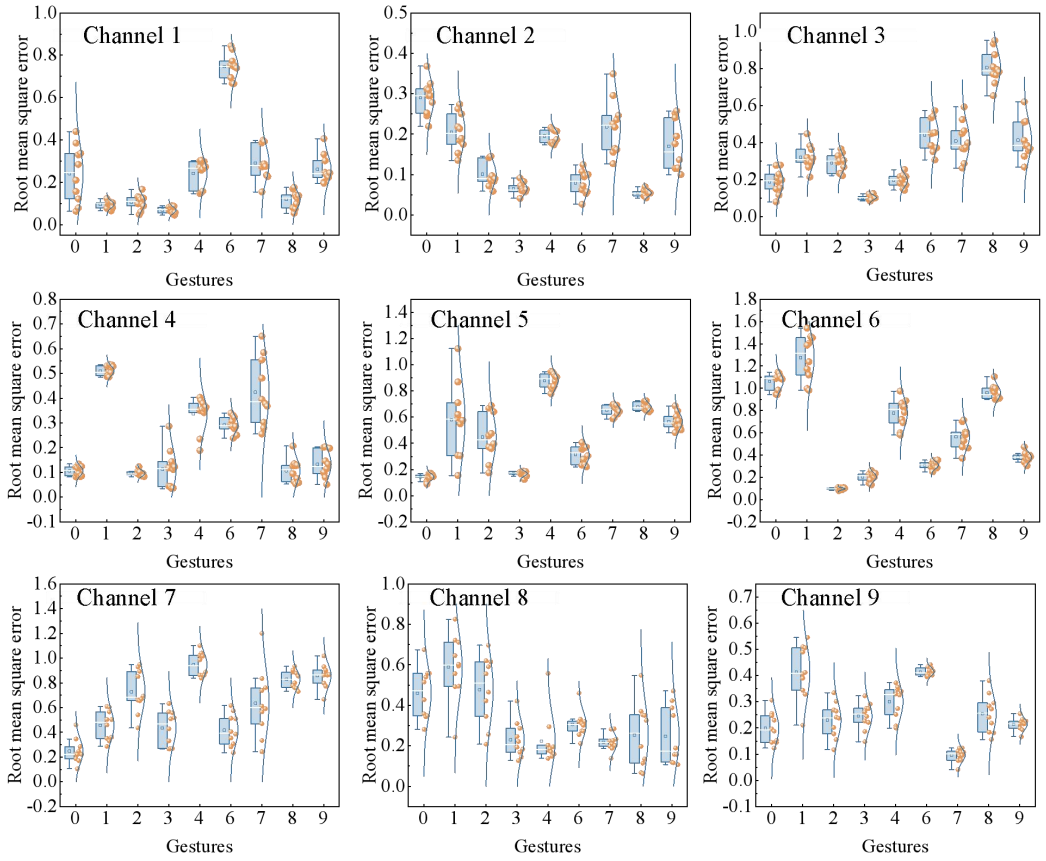

Supplementary Figure 24. RMS of different channels for different hand movement detection.

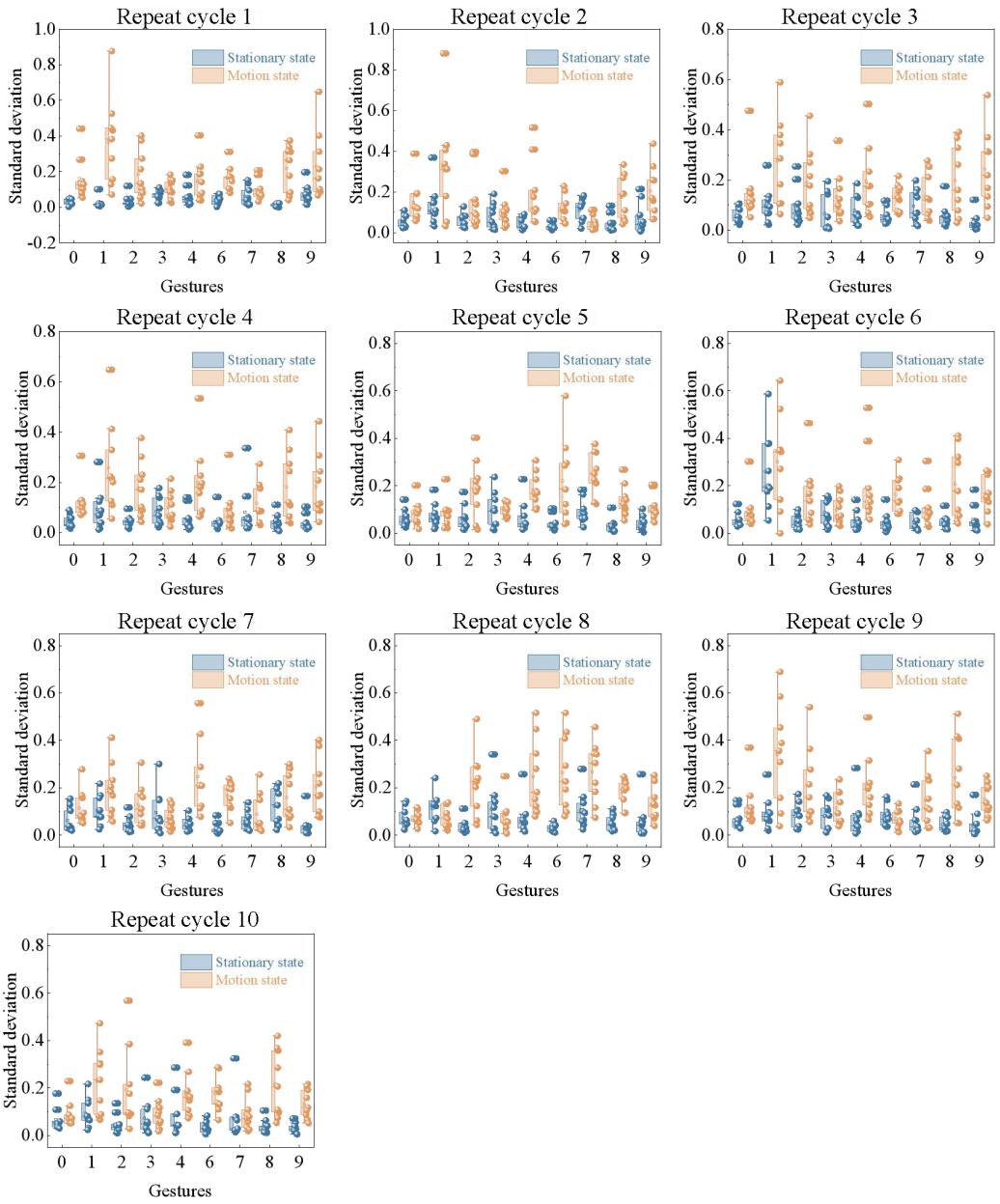

Supplementary Figure 25. Standard deviation of the rate of change of the output signals for 10 repetition cycles in steady state and kinematic state.

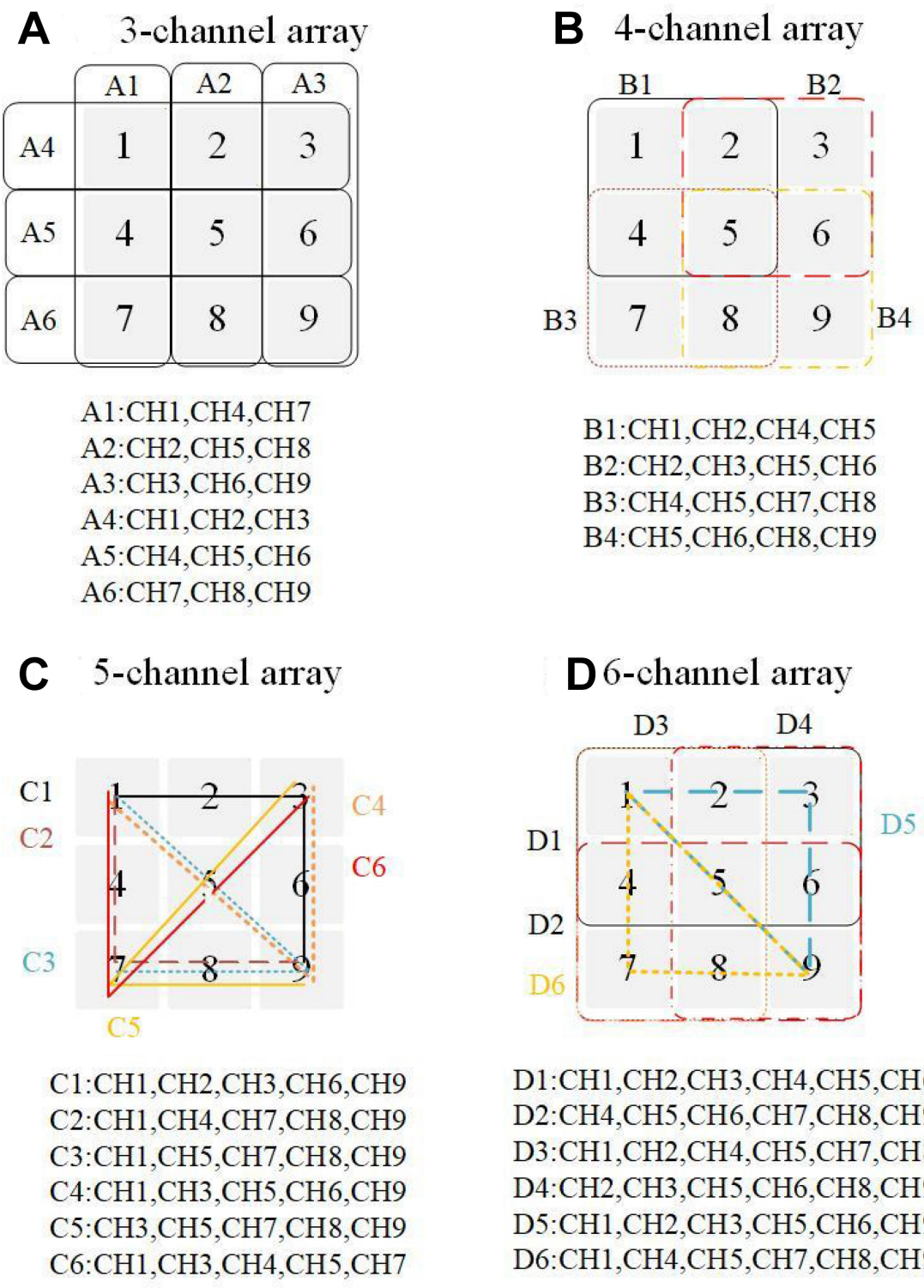

Supplementary Figure 26. Extracted from the original 9-channel array (A) 3-channel array, (B) 4-channel array, (C) 5-channel array, (D) 6-channel array.

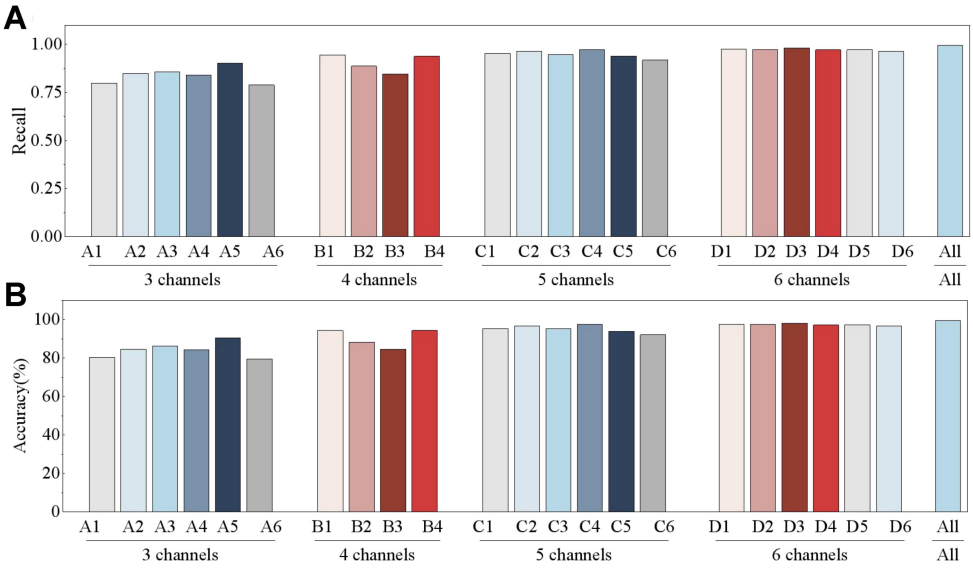

Supplementary Figure 27. (A) Recall and (B) Accuracy of classification prediction with different number of channels.

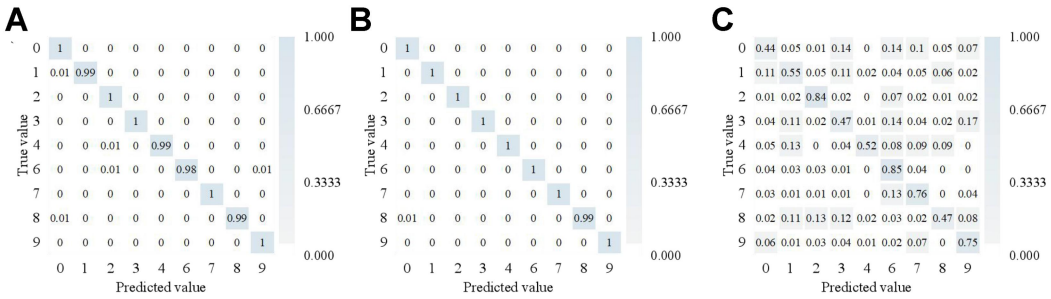

Supplementary Figure 28. Confusion matrix for classification prediction of (A) original data, (B) low-pass filtered data and (C) high-pass filtered data.

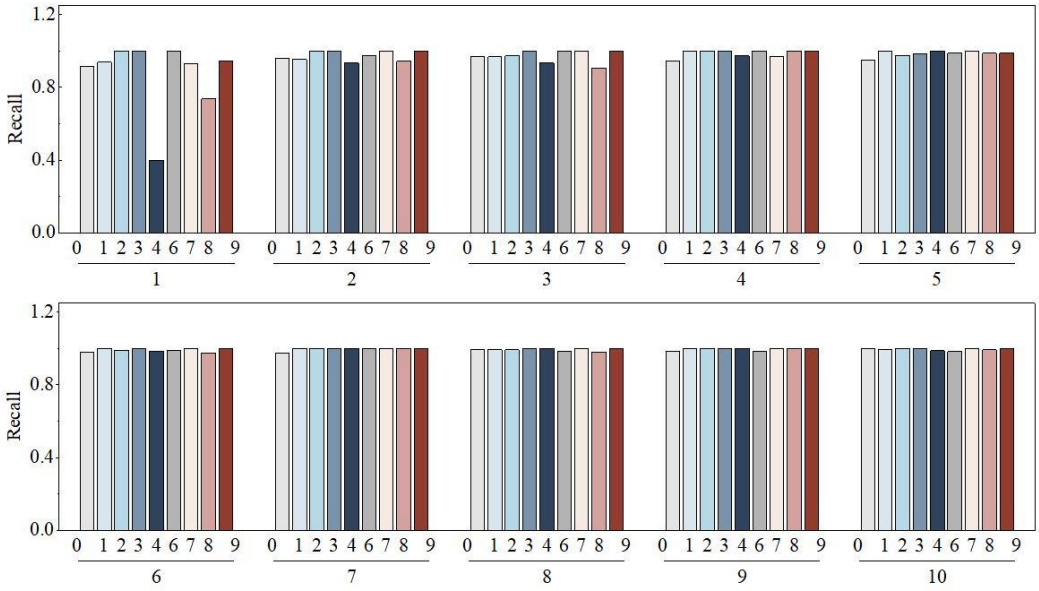

Supplementary Figure 29. Recall of predictions made with different amounts of data.

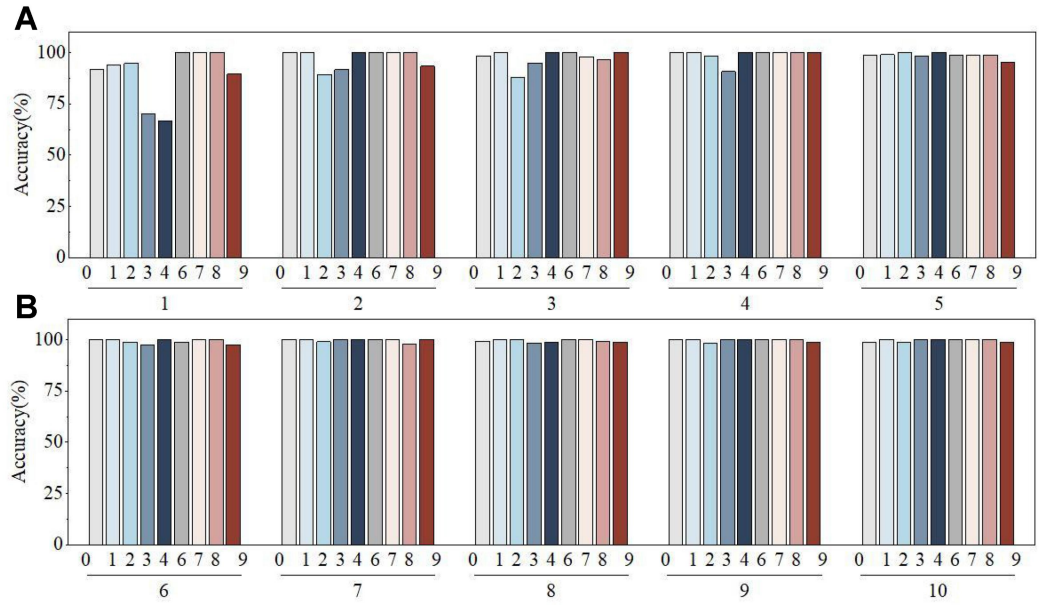

Supplementary Figure 30. Accuracy of predictions made with different amounts of data.

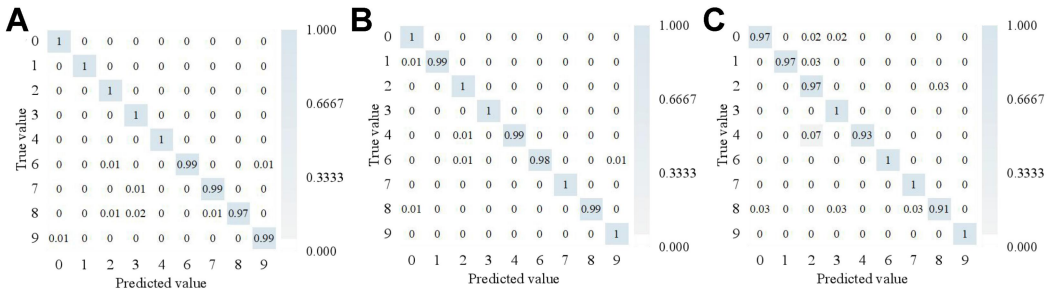

Supplementary Figure 31. Confusion matrix for categorical prediction of (A) slow, (B) normal speed and (C) fast hand movement data.

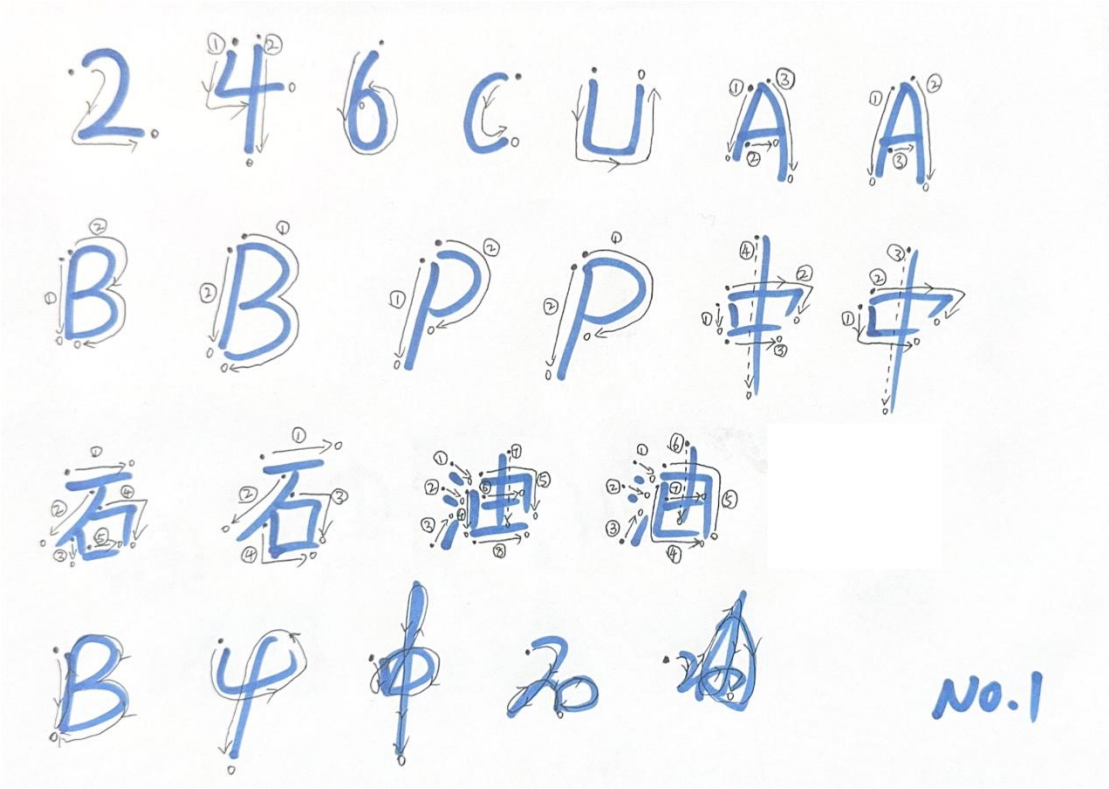

Supplementary Figure 32. Write the writing samples for each character category of Volunteer No.1. Where • indicates the starting point of the writing, o indicates the ending point, → indicates the direction of the writing, and ①②③… indicates the stroke sequence.

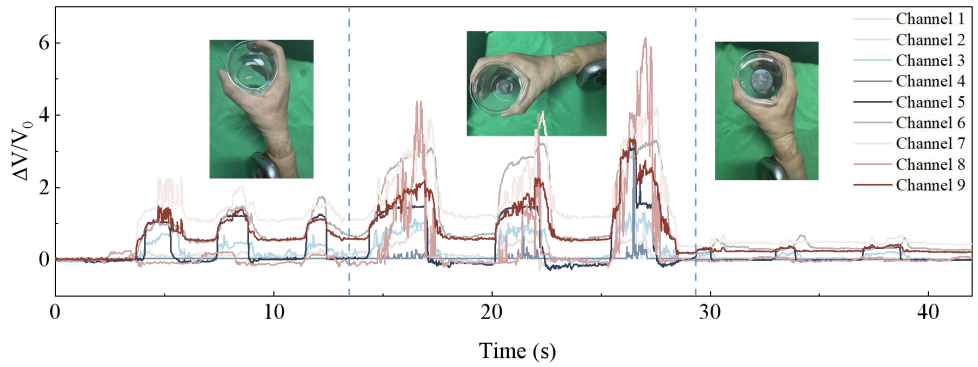

Supplementary Figure 33. Response curves for holding different weights.

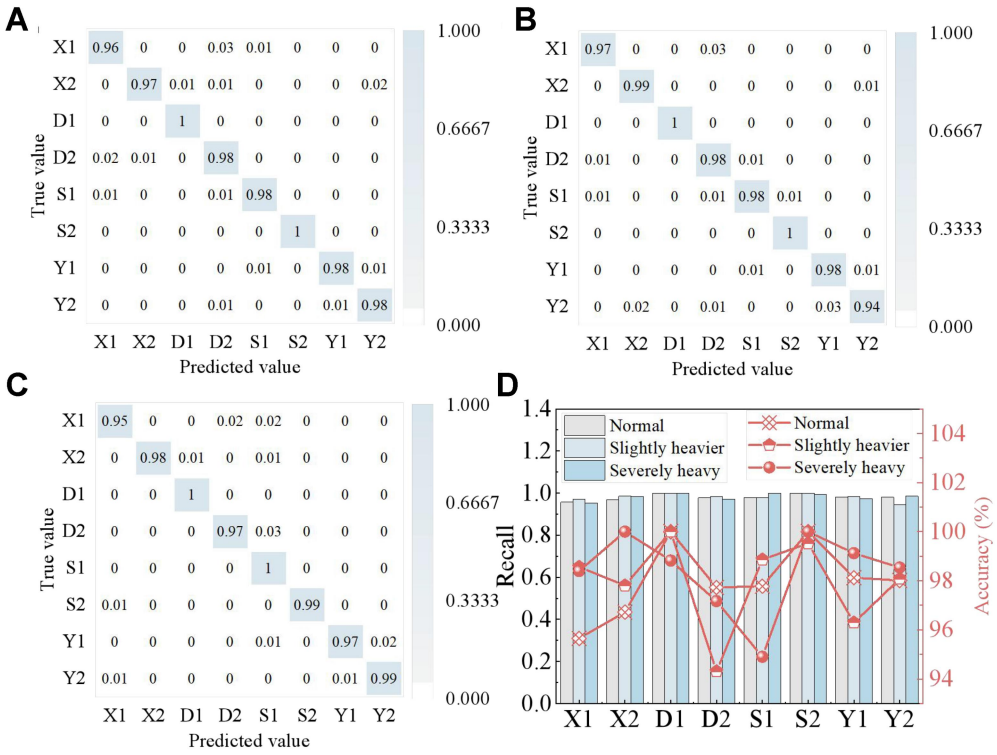

Supplementary Figure 34. (A) Confusion matrix for normal heavy pens, (B) Confusion matrix for slightly heavier pens, (C) Confusion matrix for heavier pens, (D) The classification recall and accuracy of writing symbols with different weights of pens.

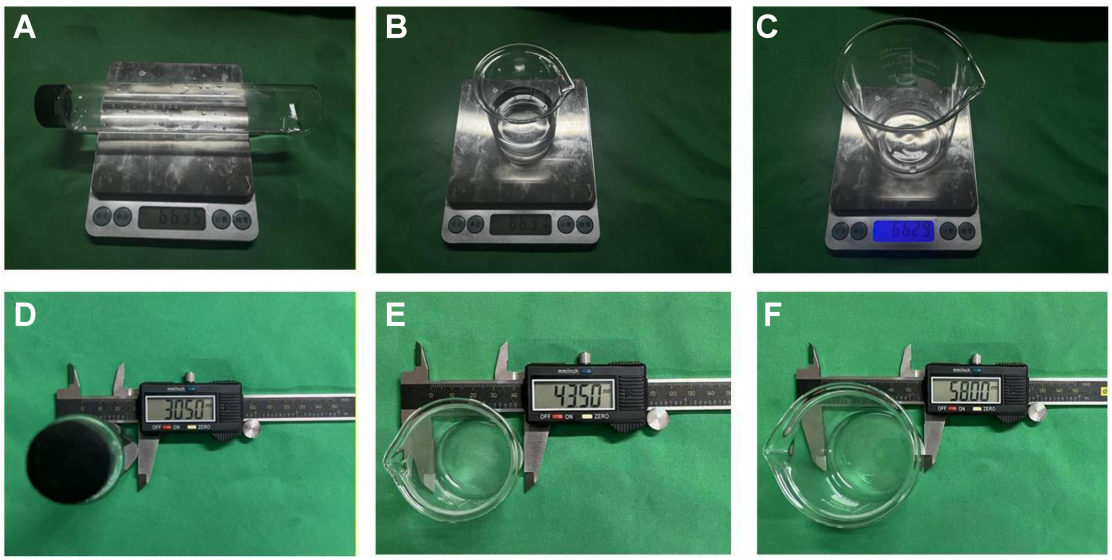

Supplementary Figure 35. Beakers of the same mass and different diameters. The beakers of different diameters have different masses, and water is added to the smaller mass so that all three beakers have the same mass.

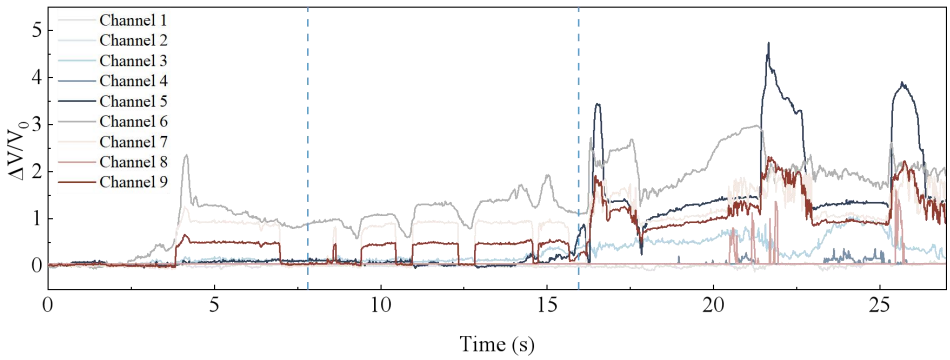

Supplementary Figure 36. Response curves for holding objects of different diameters.

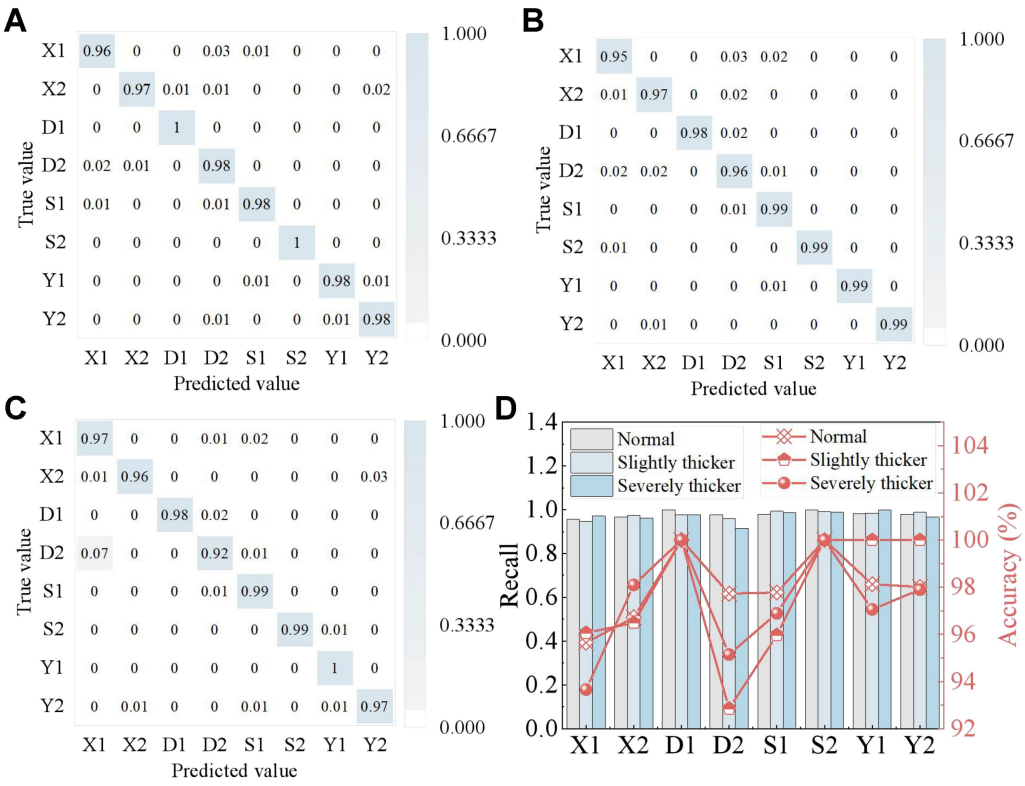

Supplementary Figure 37. (A) Confusion matrix for normal thick and thin pens, (B) confusion matrix for slightly thicker pens, (C) confusion matrix for even thicker pens, (D) The classification recall and accuracy of writing symbols with different thicknesses of pens.

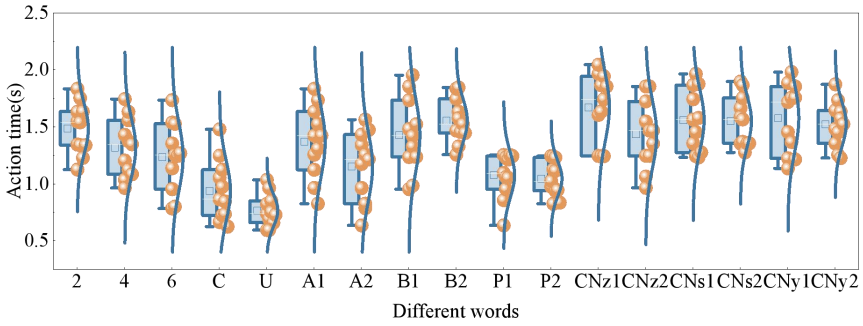

Supplementary Figure 38. Time to write different words.

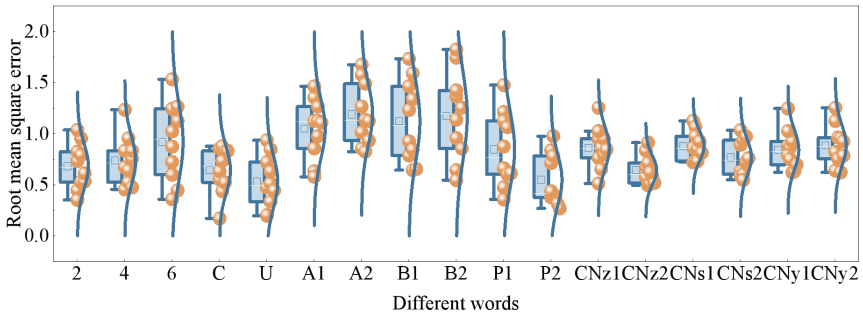

Supplementary Figure 39. RMS for writing different words.

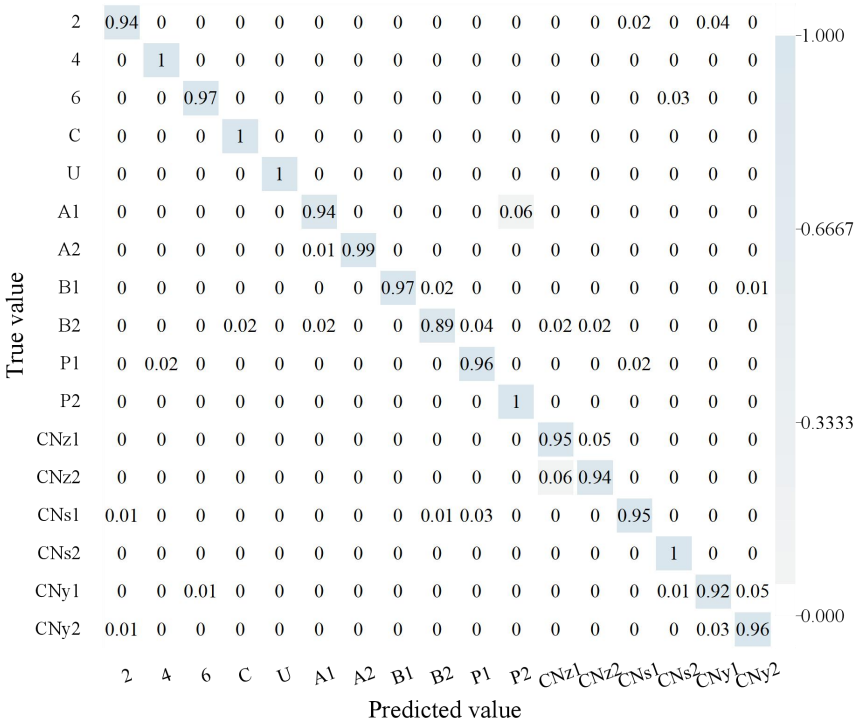

Supplementary Figure 40. Categorical confusion matrix for writing different alphabets.

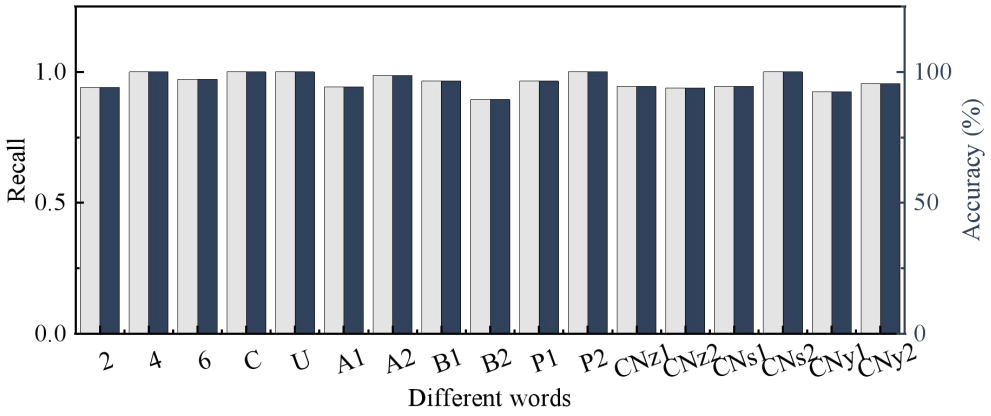

Supplementary Figure 41. Recall and accuracy of classification for writing different letters of the alphabet.

Supplementary Figure 42. Confusion matrix for 26 alphabet handwriting recognition based on a single-subject dataset.

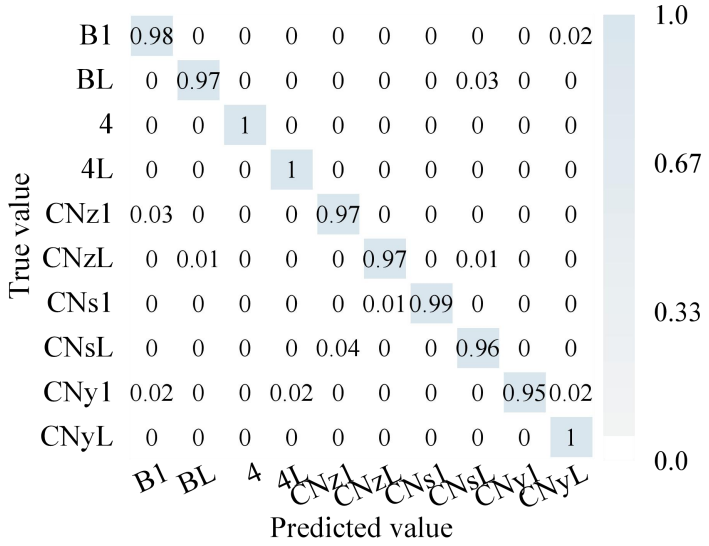

Supplementary Figure 43. Confusion matrix for categorization of normal and legato writing.

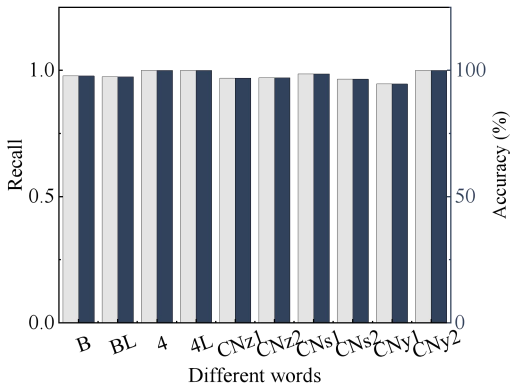

Supplementary Figure 44. Recall and accuracy for normal and continuous writing classification.

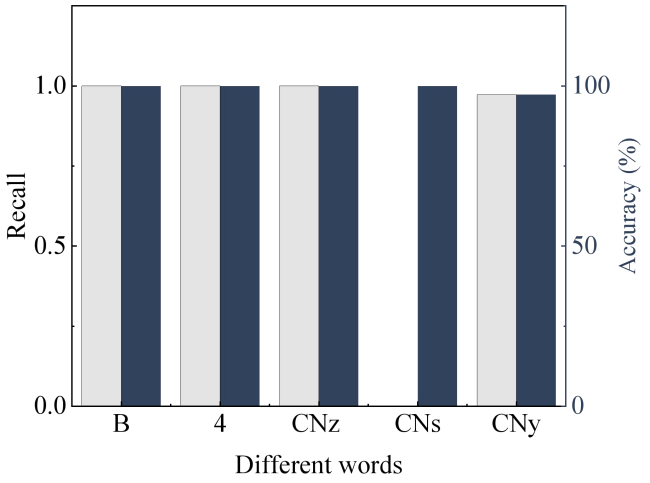

Supplementary Figure 45. Accuracy and recall rate of mixed dataset classification.

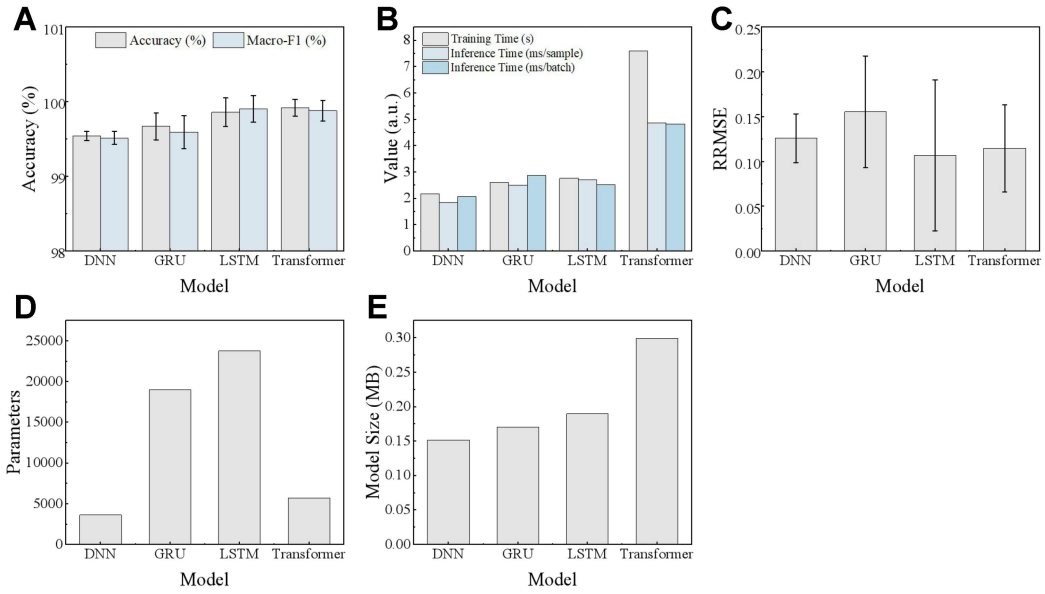

Supplementary Figure 46. (A) Accuracy and Macro-F1 comparison, error bars represent the standard deviation obtained from five-fold cross-validation. (B) Training time and inference time comparison. (C) RRMSE comparison, error bars represent the standard deviation obtained from five-fold cross-validation. (D) Trainable parameters comparison. (E) Model size comparison. Error bars represent standard deviation across cross-validation folds.

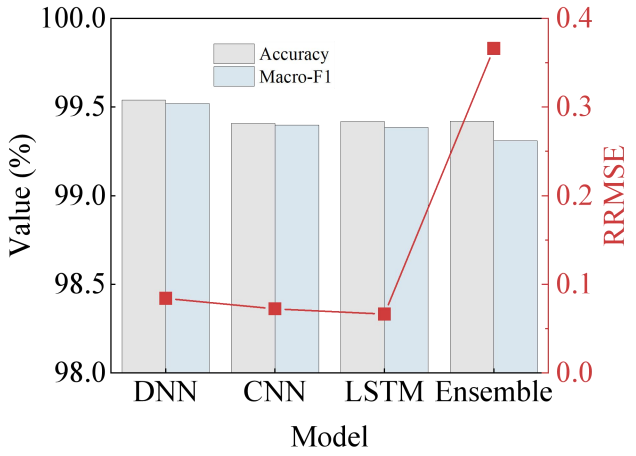

Supplementary Figure 47. Comparison of different machine learning architectures under the same training protocol. The evaluated models include a fully connected deep neural network (DNN), a one-dimensional convolutional neural network (1D-CNN), a long short-term memory network (LSTM), and an ensemble learning model. All models were trained and evaluated using the same preprocessing procedure and five-fold cross-validation protocol.

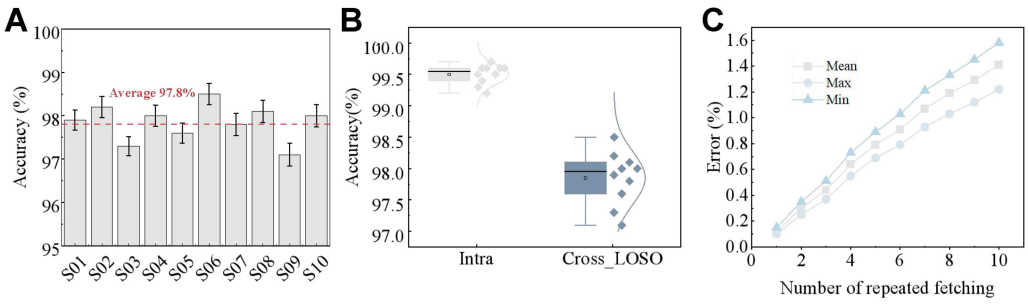

Supplementary Figure 48. Cross-subject validation and recalibration stability of the flexible sensing system. (A) Cross-subject accuracy under LOSO protocol, error bars represent the standard deviation obtained from five-fold cross-validation. Bar chart showing recognition accuracy for ten subjects using leave-one-subject-out validation (97–99 %), confirming inter-individual robustness. (B) Comparison of intra-subject and cross-subject accuracies. Box or paired-dot plot comparing individual-specific and cross-subject results, showing a small drop from 99.5 % to 97.8 % while maintaining high generalization. (C) Baseline drift during repeated attachment cycles. Line chart showing cumulative baseline variation (< 1.6 %) across ten attachment–detachment cycles, verifying mechanical and electrical stability of the array.

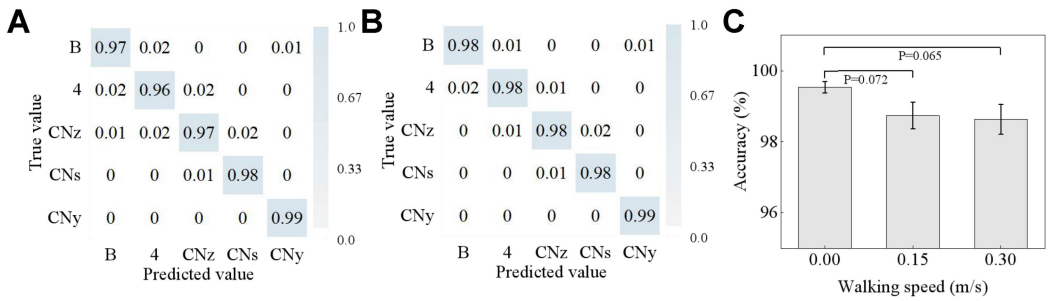

Supplementary Figure 49. (A and B) Normalized confusion matrices for classification of handwritten characters when participants performed writing while walking at approximately 0.15 m/s (slow walking) and 0.35 m/s (fast walking), respectively. The model was trained using handwriting data collected under static conditions and then tested under different walking speeds. (C) Comparison of overall classification accuracies under static, slow-walking, and fast-walking conditions. Error bars represent the standard deviation (SD) obtained from five-fold cross-validation (n = 5). Data are presented as mean ± SD. Statistical analysis was performed using MATLAB R2023b (MathWorks, Natick, MA, USA). Paired t-tests were conducted based on matched cross-validation folds. The recognition accuracies reached 98.74 ± 0.37% and 98.63 ± 0.42% for the two walking speeds, respectively, showing no statistically significant difference compared with the baseline accuracy (99.54 ± 0.16%, p = 0.072 and 0.065). These results demonstrate that the proposed FMG sensing system maintains stable performance under moderate arm motion disturbances.

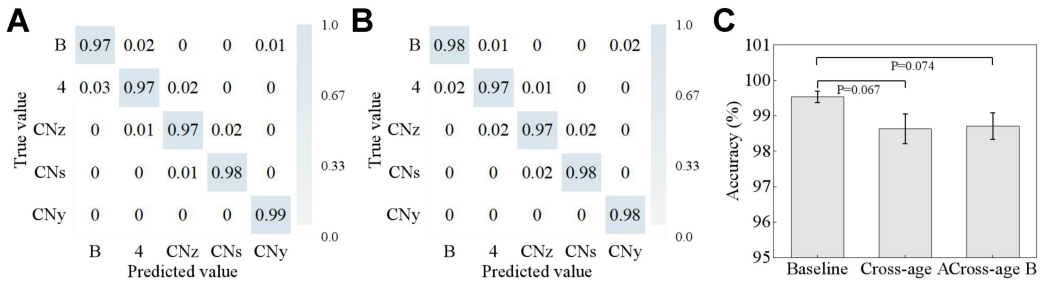

Supplementary Figure 50. Cross-age user validation of handwriting recognition. (A) Classification confusion matrix for a 41-year-old male. (B) Classification confusion matrix for a 46-year-old female. (C) Comparison of classification results across different datasets. Error bars represent the standard deviation (SD) obtained from five-fold cross-validation (n = 5). Data are presented as mean ± SD. Statistical analysis was performed using MATLAB R2023b (MathWorks, Natick, MA, USA). Paired t-tests were conducted based on matched cross-validation folds. Normalized confusion matrices were obtained from two participants over 40 years of age. The model was trained using the original dataset collected from younger adult participants (22 ± 2 years) and tested directly on handwriting data from two older participants without subject-specific fine-tuning. The overall recognition accuracies were 98.63 ± 0.42% and 98.71 ± 0.38%, respectively, which were not statistically significant compared to the baseline accuracies (99.54 ± 0.16%, paired t-test, p = 0.067 and 0.074).

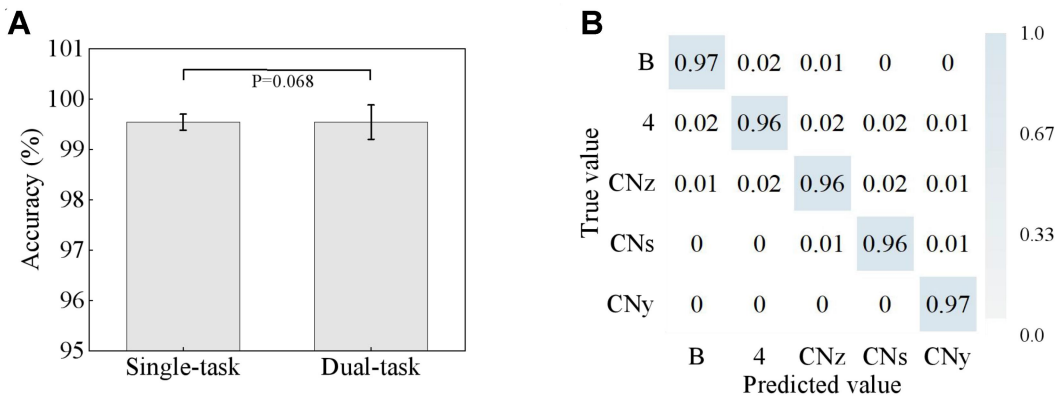

Supplementary Figure 51. (A) Classification accuracy under single-task and dual-task conditions. Error bars represent the standard deviation (SD) obtained from five-fold cross-validation (n = 5). Data are presented as mean ± SD. Statistical analysis was performed using MATLAB R2023b (MathWorks, Natick, MA, USA). Paired t-tests were conducted based on matched cross-validation folds. (B) Confusion matrix obtained under the dual-task condition. To evaluate the robustness of the proposed FMG-based handwriting recognition system under attention fluctuation, a dual-task experiment was conducted in which participants performed handwriting while simultaneously carrying out a serial subtraction task. As shown in Figure S51(A), the average classification accuracy decreased slightly from 99.54 ± 0.11% in the single-task condition to 97.65 ± 0.34% in the dual-task condition (, p = 0.068), indicating that the cognitive load introduces a modest performance reduction. However, the overall accuracy remained above 97%, demonstrating the robustness of the proposed sensing and decoding framework. The confusion matrix in Figure S51(B) further shows that most predictions remain concentrated along the diagonal, suggesting that the dominant classification patterns are preserved even when attention is partially diverted.

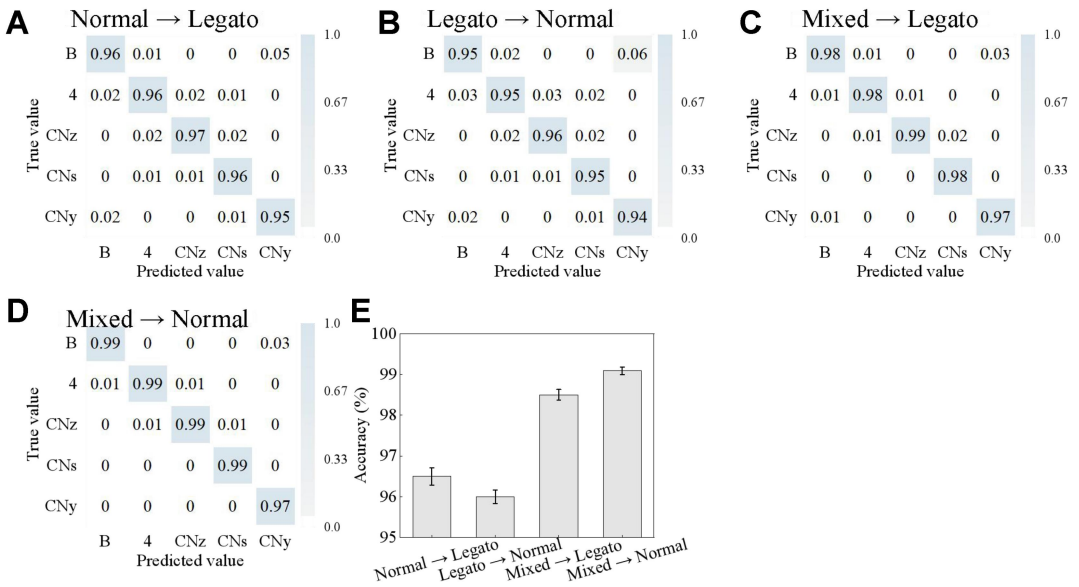

Supplementary Figure 52. (A-D), Classification accuracy under different train–test continuity conditions, including normal-to-legato, legato-to-normal, mixed-to-legato, and mixed-to-normal settings. (E) Generalization performance comparison. Error bars represent the standard deviation (SD) obtained from five-fold cross-validation (n = 5). When the model was trained using normal handwriting samples and tested on legato handwriting samples (Normal → Legato), the recognition accuracy reached 96.5 ± 0.21%, indicating that the model maintained relatively high performance even when encountering connected handwriting patterns. When the training and testing conditions were reversed (Legato → Normal), the accuracy was 96.0 ± 0.17%, showing a similar level of cross-style generalization. After introducing mixed handwriting samples for training, the performance improved significantly. The accuracy increased to 98.5 ± 0.13% under the Mixed → Legato condition and further reached 99.09 ± 0.09% for Mixed → Normal. These results demonstrate that incorporating diverse handwriting styles during training effectively enhances the robustness and generalization capability of the proposed FMG-based handwriting recognition system.

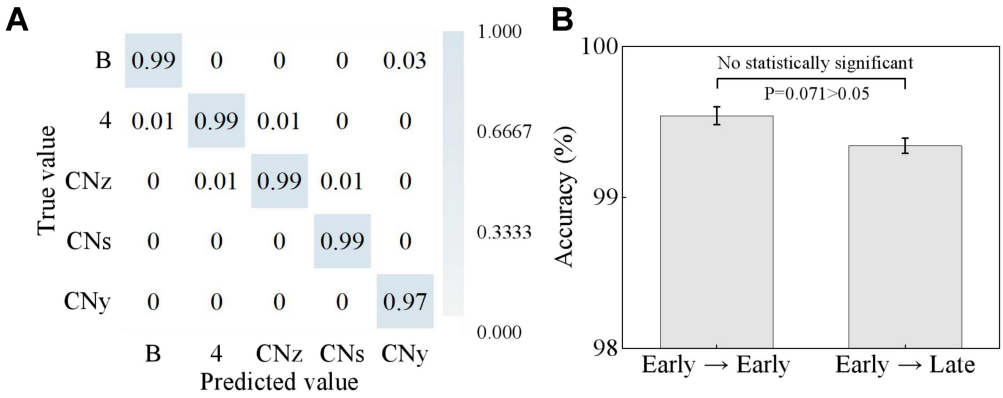

Supplementary Figure 53. (A), Confusion matrix for temporal cross-validation (Early → Late condition). (B) Comparison of classification accuracy between Early → Early and Early → Late conditions. Error bars represent the standard deviation obtained from five-fold cross-validation (n = 5). Data are presented as mean ± SD. Statistical analysis was performed using MATLAB R2023b (MathWorks, Natick, MA, USA). Paired t-tests were conducted based on matched cross-validation folds. When both training and testing samples were selected from the early stage of the writing session (Early → Early), the recognition accuracy reached 99.54 ± 0.06%. When the model was trained using early samples and tested on later samples within the same writing session (Early → Late), the accuracy remained 99.34 ± 0.05%. Statistical analysis using a paired t-test showed no significant difference between the two conditions ($p = 0.071$), indicating that temporal variations during the writing session have minimal influence on recognition performance. These results demonstrate that the proposed FMG-based handwriting recognition framework exhibits strong temporal stability and generalization capability.

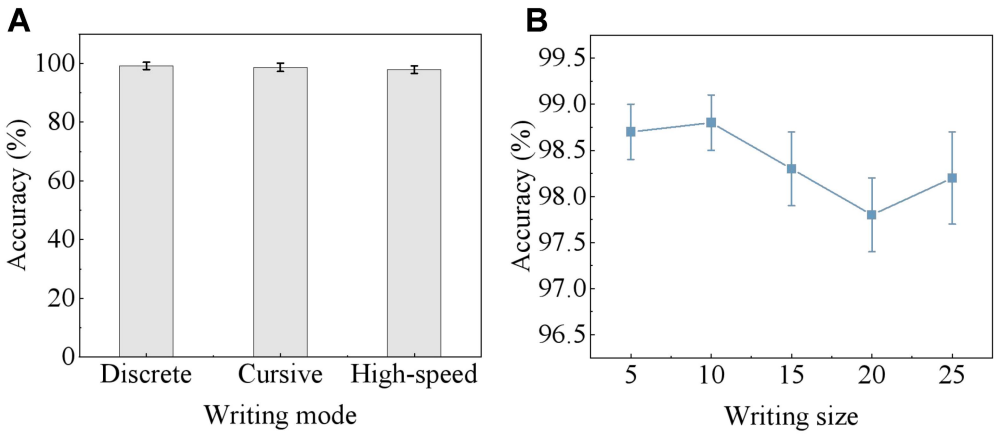

Supplementary Figure 54. Robustness of handwriting recognition to continuity, style, and scale. (A) Recognition performance under discrete, cursive, and high-speed stylized handwriting, showing only <1.5 % accuracy drop compared with discrete characters; (B) Recognition accuracy as a function of handwriting size (5–25 mm character height), remaining >97 % across all scales, confirming geometric robustness of muscle deformation signatures. Error bars represent the standard deviation (SD) obtained from five-fold cross-validation (n = 5).

Supplementary Table 1. Comparison of performance of flexible film sensors

Ref.	Max sensitivity (kPa^{-1})	Linearity (R^2)	Range (kPa)	Response/Recovery Time (ms)	Stability (cycles)	LOD
2	0.164	NG	60	100/100	1000	NG
8	0.74	NG	300	50/60	>20000	NG
S1	3.2	0.98	50	20/20	5000	5 Pa
S2	0.85	0.995	500	30/35	10000	2 Pa
S2	1.9	NG	150	10/15	>10000	10 Pa
S4	0.62	0.99	300	40/45	8000	3 Pa
S5	0.45	0.997	1000	25/30	>20000	1 Pa
S6	2.8	NG	80	15/20	6000	8 Pa
S7	1.12	0.992	200	18/20	>10000	2 Pa
S8	5.6	NG	30	8/10	5000	0.8 Pa
S9	0.95	0.996	400	25/30	>15000	1.5 Pa
S10	2.4	NG	120	12/15	8000	3 Pa
S11	0.78	0.991	600	40/50	>20000	2 Pa
S12	1.85	0.994	250	20/25	10000	1 Pa
S13	1.25	0.993	294	30/15	10000	0.6
S14	45.7 mV/Pa	NG	1.2	<5/NG	40000	NG
S15	10.29	NG	9	~30/NG	10000	5 mg
S16	2.1	NG	25	100/100	2000	NG
S17	1.675	NG	2000	120/120	>1500	NG
S18	0.6275	NG	166	120/60	10000	1 g
This work	1.364	0.9982	100	12/16	>3000	9.74 Pa

Supplementary Table 2. Performance comparison of different models

Model	Accuracy (%)	Std	Macro-F1 (%)	Std	RRMSE	Std	Training Time (s)	Inference Time (ms/sample)	Inference Time (ms/batch)	Parameters	Model Size (MB)
DNN	99.54	0.16	99.52	0.19	0.13	0.027	2.17	1.84	2.08	3610	0.15
GRU	99.67	0.89	99.59	0.87	0.16	0.062	2.61	2.50	2.87	19018	0.17
LSTM	99.86	0.97	99.90	0.998	0.11	0.084	2.76	2.70	2.51	23754	0.19
Transformer	99.92	1.13	99.88	1.14	0.11	0.049	7.59	4.87	4.82	5706	0.30

Supplementary Table 3. Ablation study on the depth of the DNN architecture

Configuration	Accuracy (%)	Macro-F1 (%)
1 hidden layer	94.67	94.59
2 hidden layers	97.29	97.40
3 hidden layers	99.54	99.52

As the number of hidden layers increases, the model's capability to capture nonlinear features in force myography (FMG) signals is progressively enhanced, leading to improvements in both classification accuracy and Macro-F1 score. The optimal performance is achieved with a three-layer architecture, while further increasing network complexity provides limited performance gains and may introduce overfitting. Therefore, a three-layer Deep Neural Network (DNN) is adopted as the final model for handwriting recognition.

Supplementary Table 4. Ablation study on normalization and regularization

Configuration	Accuracy (%)	Macro-F1 (%)
Full DNN	99.54	99.52
w/o BN	97.82	97.85
w/o Dropout	97.75	97.73
w/o BN & Dropout	97.10	97.11

To evaluate the effect of regularization modules on model performance, ablation studies were conducted on Batch Normalization and Dropout. The results show that the full DNN model achieves the best performance in terms of accuracy and Macro-F1 score, while also exhibiting the lowest relative root mean square error (RRMSE). Removing either Batch Normalization or Dropout leads to noticeable performance degradation, and removing both results in the most significant decline. These findings indicate that both modules effectively improve training stability and enhance model generalization.

Supplementary Table 5. Comparison of representative sEMG and FMG based gesture-recognition systems with this work

No.	Sensing Modality	Sensing Material / Type	Channel	Gesture Classes	Accuracy (%)	Model	Ref.
1	sEMG	Ag/AgCl wet electrodes (Myo Armband)	8	6	91	SVM / kNN	43
2	sEMG	Dry flexible Ag/AgCl electrode array	10	8	94	SVM	44
3	sEMG	Graphene-textile dry electrodes	12	10	95	ANN	S19
4	FMG	Piezoelectret film strap	8	9	93	RF/SVM	S20
5	FMG	Strain-gauge elastic band	6	10	95	kNN	S21
6	FMG	Piezoresistive silicone array	12	10	96	DT / RF	S22
7	FMG	TENG-based textile band	8	8	96	DNN	S23
8	Hybrid sEMG + FMG	Multi-modal armband (sEMG + pressure)	16	10	97	CNN	S24
9	This work (FMG)	MWCNTs/mPDMS flexible array	9	10	99.54	DNN	This study

Supplementary Table 6. Comparison of gesture recognition performance of flexible sensors

Ref.	Sensor Type	Modality	Channels	Accuracy (%)	Motion Type	Features
This work	FMG array (mPDMS/MWCNTs)	Pressure	9	99.54	Handwriting + gesture	High spatial resolution, wearable
S25	Soft sensing array	FMG + MMG	8–16	~96–98	Gesture	Multimodal sensing
S26	Graphene/CNT sensor	Strain	4–8	~95–97	Gesture	ML-assisted
S27	TENG array	Pressure	>16	~94–96	Gait/gesture	Self-powered
S28	Carbon aerogel	Pressure	4–12	~93–97	Gesture	Ultralight
S29	Hybrid sensor	Pressure	6–12	~95–98	Motion	Self-powered
S30	Pressure array	Pressure	8–16	~94–97	Gait/gesture	ML decoding
S31	Pressure array	Pressure	6–12	~92–95	Pulse/gesture	Wearable
S32	TENG	Pressure	4–8	~90–95	Motion	Self-powered
S33	Pressure	Pressure	6–10	~93–96	Motion	Porous structure
S34	Kirigami sensor	Pressure	4–9	~94–97	Motion	Stretchable

REFERENCES

[S1]Y. Hou, L. Wang, R. Sun, Y. Zhang, M. Gu, Y. Zhu, Y. Tong, X. Liu, Z. Wang, J. Xia, Y. Hu, L. Wei, C. Yang, M. Chen, Crack-across-pore enabled high-performance flexible pressure sensors for deep neural network enhanced sensing and human action recognition, ACS Nano 16(5) (2022) 8358–8369. https://doi.org/10.1021/acsnano.2c02609.

[S2]M. Gu, B. Zhao, J. Gao, X. Zhou, L. Huang, J. Wang, L. Wei, C. Yang, M. Chen, Nested-cell architecture and molecular surface modification enabled high-pressure range flexible sensors for extreme environments, Advanced Functional Materials 34(33) (2024) 2400494. https://doi.org/10.1002/adfm.202400494.

[S3]L. Xu, Z. Zhang, F. Gao, X. Zhao, X. Xun, Z. Kang, Q. Liao, Y. Zhang, Self-powered ultrasensitive pulse sensors for noninvasive multi-indicators cardiovascular monitoring, Nano Energy 81 (2021) 105614. https://doi.org/10.1016/j.nanoen.2020.105614.

[S4]Z. Gao, Q. Zhang, Y. Wang, W. Zhang, J. Liu, D. Xu, X. Xia, S. Hu, B. Bian, Y. Zhao, Y. Wu, Y. Liu, J. Shang, R.-W. Li, 3D printing wide detection range and high sensitivity flexible pressure sensor and its applications, Chemical Engineering Journal 196 (2024) 105840. https://doi.org/10.1016/j.reactfunctpolym.2024.105840.

[S5]Y. Ren, Z. Liu, G. Jin, M. Yang, Y. Shao, W. Li, Y. Wu, L. Liu, F. Yan, Electric-field-induced gradient ionogels for highly sensitive, broad-range-response, and freeze/heat-resistant ionic fingers, Advanced Materials 33(12) (2021) e2008486. https://doi.org/10.1002/adma.202008486.

[S6]W. Hong, X. Guo, T. Zhang, A. Zhang, Z. Yan, X. Zhang, X. Li, Y. Guan, D. Liao, H. Lu, H. Liu, J. Hu, Y. Niu, Q. Hong, Y. Zhao, Flexible capacitive pressure sensor with high sensitivity and wide range based on a cheetah-leg structure via 3D printing, ACS Applied Materials & Interfaces 15(39) (2023) 46347–46356. https://doi.org/10.1021/acsami.3c09841.

[S7]K. Meng, X. Xiao, Z. Liu, S. Shen, T. Tat, Z. Wang, C. Lu, W. Ding, X. He, J. Yang, J. Chen, Kirigami-inspired pressure sensors for wearable dynamic cardiovascular monitoring, Advanced Materials 34(36) (2022) e2202478. https://doi.org/10.1002/adma.202202478.

[S8]S. Zhang, W. Feng, Y. Jiang, Y. Li, Y. Liu, D. Yu, W. Wang, Flexible pressure sensor based on 3D printing MXene@dual-scale porous polymer, Chemical Engineering Journal 498 (2024) 155356. https://doi.org/10.1016/j.cej.2024.155356.

[S9]P. Zhang, X. Zhang, M. Teng, L. Li, X. Liu, J. Feng, W. Wang, X. Wang, X. Luo, Leather-based shoe soles for real-time gait recognition and automatic remote assistance using machine learning, ACS Applied Materials & Interfaces 16(45) (2024) 62803–62816. https://doi.org/10.1021/acsami.4c16505.

[S10] H. Zhao, Y. Zhang, L. Han, W. Qian, J. Wang, H. Wu, J. Li, Y. Dai, Z. Zhang, C. R. Bowen, Y. Yang, Intelligent recognition using ultralight multifunctional nano-layered carbon aerogel sensors with human-like tactile perception, Nano-Micro Letters 16(1) (2023) 11. https://doi.org/10.1007/s40820-023-01216-0.

[S11] H. Wu, X. Luo, C. Wang, Q. Jin, Y. Li, F. Guo, W. Guo, Y. Long, 3D printing of robust, self-healing, and highly sensitive pressure sensor based on an interpenetrating polymer network elastomer, Colloids and Surfaces A: Physicochemical and Engineering Aspects 685 (2024) 133248. https://doi.org/10.1016/j.colsurfa.2024.133248.

[S12] X. Guo, J. Zhao, B. Hu, J. Li, J. Tao, Y. Chen, S. Zong, W. Hong, X. Li, S. Zhu, S. Yu, W. Xu, Y. Zhao, Q. Hong, T. Song, Flexible pressure sensor with high sensitivity and fast response based on bionic honeycomb-structured PDMS/Al2O3 composites via 3D printing, IEEE Transactions on Electron Devices 71(7) (2024) 4283–4291. https://doi.org/10.1109/TED.2024.3401653

[S13] R. Qin, M. Hu, X. Li, T. Liang, H. Tan, J. Liu, G. Shan, A new strategy for the fabrication of a flexible and highly sensitive capacitive pressure sensor, Microsyst Nanoeng 7 (2021) 100. https://doi.org/10.1038/s41378-021-00327-1.

[S14] K. Meng, J. Chen, X. Li, Y. Wu, W. Fan, Z. Zhou, Q. He, X. Wang, X. Fan, Y. Zhang, J. Yang, Z.L. Wang, Flexible Weaving Constructed Self-Powered Pressure Sensor Enabling Continuous Diagnosis of Cardiovascular Disease and Measurement of Cuffless Blood Pressure, Advanced Functional Materials 29(5) (2018). https://doi.org/10.1002/adfm.201806388.

[S15] L. Xu, Z. Zhang, F. Gao, X. Zhao, X. Xun, Z. Kang, Q. Liao, Y. Zhang, Self-powered ultrasensitive pulse sensors for noninvasive multi-indicators cardiovascular monitoring, Nano Energy 81 (2021). https://doi.org/10.1016/j.nanoen.2020.105614.

[S16] M. Wang, G. Wang, M. Zheng, L. Liu, C. Xu, Z. Liu, L. He, High-performance flexible piezoresistive pressure sensor based on multi-layer interlocking microstructures, Journal of Materials Chemistry A 12(34) (2024) 22931-22944. https://doi.org/10.1039/d4ta03758h.

[S17] L. Huang, S. Wang, P. Zhang, K. Zhang, Y. Li, Z. Chen, A Flexible Pressure Sensor with Wide Detection Range Based on Capacitive-Piezoresistive Dual Mode Conversion for Human-Machine Interaction, Advanced Materials Technologies 9(4) (2024). https://doi.org/10.1002/admt.202301377.

[S18] J. Tan, P. Zhang, K. Zhang, X. Bu, G. Dou, L. Huang, Fabrication of Flexible Capacitive Pressure Sensors by Adjusting the Height of the Interdigital Electrode, ACS Applied Electronic Materials 6(6) (2024) 4539-4547. https://doi.org/10.1021/acsaelm.4c00586.

[S19] Y. Li, T. Chen, X. Zhao, J. Zhou, Flexible graphene–textile dry electrodes for long-term and high-fidelity surface electromyography recording, *ACS Applied Electronic Materials* **3**(9) (2021) 3924–3932. https://doi.org/10.1021/acsaelm.1c00326.

[S20] S. Park, J. H. Lee, C. Kim, Piezoelectret-based force myography strap for gesture recognition and prosthetic control, *IEEE Transactions on Neural Systems and Rehabilitation Engineering* **28**(12) (2020) 3114–3123. https://doi.org/10.1109/TNSRE.2020.3031554

[S21] L. Huang, P. Wang, X. Zhang, High-precision hand motion detection using strain-gauge-based force myography, *Sensors and Actuators A: Physical* **331** (2021) 112985. https://doi.org/10.1016/j.sna.2021.112985.

[S22] C. Wu, Y. Xu, H. Zhao, Y. Wang, Triboelectric textile band for dynamic muscle force monitoring and gesture classification, Nano Energy 107 (2023) 108163. https://doi.org/10.1016/j.nanoen.2023.108163.

[S23] D. Kim, S. Park, Hybrid armband integrating sEMG and pressure sensors for multi-modal human–machine interfaces, *IEEE Transactions on Biomedical Circuits and Systems* **17**(1) (2023) 55–66. https://doi.org/10.1109/TBCAS.2023.3234567

[S24] Y. Zhang, M. Wang, Q. Chen, Bio-inspired flexible piezoresistive array for dynamic muscle force reconstruction and gesture recognition, *Biosensors and Bioelectronics* **210** (2022) 114282. https://doi.org/10.1016/j.bios.2022.114282

[S25] J. Suo, Y. Liu, J. Wang, M. Chen, K. Wang, X. Yang, K. Yao, V. A. L. Roy, X. Yu, W. A. Daoud, N. Liu, J. Wang, Z. Wang, W. J. Li, AI-enabled soft sensing array for simultaneous detection of muscle deformation and mechanomyography for metaverse somatosensory interaction, Advanced Science 11(16) (2024) e2305025. https://doi.org/10.1002/advs.202305025.

[S26] H. Y. Shen, Y. T. Li, H. Liu, J. Lin, L. Y. Zhao, G. P. Li, Y. W. Wu, T. L. Ren, Y. Wang, Machine learning-assisted gesture sensor made with graphene/carbon nanotubes for sign language recognition, ACS Applied Materials & Interfaces 16(39) (2024) 52911–52920. https://doi.org/10.1021/acsami.4c10872.

[S27] H. Zhou, Y. Gui, G. Gu, H. Ren, W. Zhang, Z. Du, G. Cheng, A plantar pressure detection and gait analysis system based on flexible triboelectric pressure sensor array and deep learning, Small 21(1) (2025) e2405064. https://doi.org/10.1002/smll.202405064.

[S28] H. Zhao, Y. Zhang, L. Han, W. Qian, J. Wang, H. Wu, J. Li, Y. Dai, Z. Zhang, C. R. Bowen, Y. Yang, Intelligent recognition using ultralight multifunctional nano-layered carbon aerogel sensors with human-like tactile perception, Nano-Micro Letters 16(1) (2023) 11. https://doi.org/10.1007/s40820-023-01216-0.

[S29] L. Zhan, J. Lv, S. Chen, A. Gupta, Y. Xin, F. Jiang, J. P. Lee, J. Xiong, N. Wang, P. S. Lee, Moisture-triggered hybrid soft actuator and electric generator for self-sensing wearables and adaptive human–environment interaction, Nano Energy 132 (2024). https://doi.org/10.1016/j.nanoen.2024.110410.

[S30] P. Zhang, X. Zhang, M. Teng, L. Li, X. Liu, J. Feng, W. Wang, X. Wang, X. Luo, Leather-based shoe soles for real-time gait recognition and automatic remote assistance using machine learning, ACS Applied Materials & Interfaces 16(45) (2024) 62803–62816. https://doi.org/10.1021/acsami.4c16505.

[S31] J. Wang, Y. Zhu, Z. Wu, Y. Zhang, J. Lin, T. Chen, H. Liu, F. Wang, L. Sun, Wearable multichannel pulse condition monitoring system based on flexible pressure sensor arrays, Microsystems & Nanoengineering 8 (2022) 16. https://doi.org/10.1038/s41378-022-00349-3.

[S32] L. Xu, Z. Zhang, F. Gao, X. Zhao, X. Xun, Z. Kang, Q. Liao, Y. Zhang, Self-powered ultrasensitive pulse sensors for noninvasive multi-indicators cardiovascular monitoring, Nano Energy 81 (2021). https://doi.org/10.1016/j.nanoen.2020.105614.

[S33] T. Xu, Q. Song, K. Liu, H. Liu, J. Pan, W. Liu, L. Dai, M. Zhang, Y. Wang, C. Si, H. Du, K. Zhang, Nanocellulose-assisted construction of multifunctional MXene-based aerogels with engineering biomimetic texture for pressure sensor and compressible electrode, Nano-Micro Letters 15(1) (2023) 98. https://doi.org/10.1007/s40820-023-01073-x.

[S34] K. Meng, X. Xiao, Z. Liu, S. Shen, T. Tat, Z. Wang, C. Lu, W. Ding, X. He, J. Yang, J. Chen, Kirigami-inspired pressure sensors for wearable dynamic cardiovascular monitoring, Advanced Materials 34(36) (2022) e2202478. https://doi.org/10.1002/adma.202202478.